FABRICATION AND CHARACTERIZATION OF SUPERCONDUCTING Bi2212 BOLOMETER FOR THE DETECTION OF THZ WAVES

A Thesis submitted to
the Graduate School of Engineering and Sciences of
İzmir Institute of Technology
in Partial Fulfillment of the Requirements for the Degree of

MASTER OF SCIENCE

in Physics

by
Metin KURT

September 2014
İZMİR

We approve the thesis of **Metin KURT**

Examining Committee Members:

_____

Assoc. Prof. Dr. Gülnur AYGÜN ÖZYÜZER
Department of Physics, Izmir Institute of Technology

_____

Prof. Dr. Lütfi ÖZYÜZER
Department of Physics, Izmir Institute of Technology

_____

Assoc. Prof. Dr. Hakan ALTAN
Department of Physics, Middle East Technical University

_____

Assoc. Prof. Dr. Ekrem ÖZDEMİR
Department of Mechanical Engineering, Izmir Institute of Technology

_____

Dr. Mehtap ÖZDEMİR KÖKLÜ
Department of Opticianry, Gediz University

12 September 2014

_____

Assoc. Prof. Dr. Gülnur AYGÜN ÖZYÜZER
Supervisor, Department of Physics,
Izmir Institute of Technology

_____

Prof. Dr. Lütfi ÖZYÜZER
Co-Supervisor,
Department of Physics,
Izmir Institute of Technology

_____

Prof. Dr. Nejat BULUT
Head of the Department of Physics

_____

Prof. Dr. R. Tugrul SENGER
Dean of the Graduate School of
Engineering and Sciences

ACKNOWLEDGMENTS

Firstly, I would like to thank my supervisor Assoc. Prof. Gülnur AYGÜN ÖZYÜZER for letting possibility to complete this thesis and helping during my M.S. studies. I would like to say my special thanks to my co-advisor Prof. Lütfi ÖZYÜZER for encouragement, his instructive guidance and bring experience me in terahertz science and technology area.

In addition, I am indebted to the thesis committee members Assoc. Prof. Hakan ALTAN, Assoc. Prof. Ekrem ÖZDEMİR and Dr. Mehtap ÖZDEMİR KÖKLÜ for their valuable comments on my thesis. Moreover, my special thanks go to Hasan KÖSEOĞLU, Mutlu D. YAMAN, Tuğçe SEMERCİ, Yasemin DEMİRHAN, who help me during my thesis because of their friendship and support whenever I need. Of course, Hasan deserves a special recognition because he always endured our endless questions with his deep knowledge of science and behaved us like a brother. Furthermore, I am grateful to Adnan TAŞDEMİR for the schematics of the experimental process were being drawn.

I would also like to acknowledge Prof. Wang from National Institute for Materials Science and Prof. Miyakawa from Tokyo University of Science for providing the Bi2212 crystals. I acknowledge this thesis was supported by Ministry of Science, Industry and Technology under project number SANTEZ 1386.STZ.2012-1 which is cooperated with ASELSAN and thanks also to Applied Quantum Research Center at Iztech providing me clean room facilities.

Finally, I can’t find better words to explain contribution of my family to my education and explain their love. I express my thanks for their helps.

ABSTRACT

FABRICATION AND CHARACTERIZATION OF SUPERCONDUCTING Bi2212 BOLOMETER FOR THE DETECTION OF THZ WAVES

Since terahertz (THz) waves can pass through materials like clothing, plastic, wood, ceramic, leather and without harm to the body, it can be used for characterization, detection and 3D imaging of these materials. THz application area expands day by day such as high-speed wireless communications, medical imaging, security in airports and shopping centres and detection of chemical and biological materials. Rapidly increasing applications of the electromagnetic waves (EM) in the under developed terahertz frequency (0.1-10 THz) range requires a well understandings of efficient terahertz wave detection. An intense, coherent and continuous electromagnetic wave source is obtained by High-T_c superconductor $Bi_2Sr_2CaCu_2O_{8+\delta}$ (Bi2212) single crystal. At the same time Bi2212 single crystal can detect THz waves in suitable conditions. Nowadays, different types of bolometers are used for detection of THz waves. But they have many limitations like slow response time which is the most significant problem and costly cryogenic spending. In this study, single crystal of Bi2212 is cleaved to layer by layer by scotch tape until the necessary is reached thickness. Afterwards, it is pasted on a sapphire substrate and the scotch tape is etched with the aid of chloroform solution and ultrasonic cleaner. After the crystal fabrication, the exact thickness of the crystal were obtained using atomic force microscopy. Then, the samples were annealed at 400^{o}C for 1 hour in order to adjust the oxygen doping level and then deposited with 150 nm Au layer by thermal evaporation. Afterwards they were annealed again at 425^{o}C for 30 minutes to decrease the contact resistivity. After clean room process, our log-periodic antenna design was formed on the crystal by using e-beam lithography and Ar-ion beam etching step by step. Finally, four probe wires were connected to the two contact paths and log-periodic antenna by silver epoxy. The temperature dependence of a-b axis resistivity (R-T) for Bi2212 single crystals were performed.

ÖZET

THZ DALGALARININ ALGILANMASI İÇİN SÜPERİLETKEN Bi2212 BOLOMETRENİN ÜRETİMİ VE KARAKTERİZASYONU

Terahertz dalgaları, kıyafet, deri, plastik, tahta, seramik ve herhangi bir zarar vermeden insan vücudundan geçebildiği için bu malzemelerin karakterizasyonunda, algılanmasında ve 3D görüntülenmesinde kullanılabilir. Hızlı kablosuz iletişim, medikal görüntüleme, havaalanlarında ve alışveriş merkezlerinde güvenlik, kimyasal ve biyolojik malzemelerin algılanması gibi terahertzin uygulama alanları günden güne genişlemektedir. Elektromanyetik spectrumun az gelişmiş bölgesinde olmasına karşın, terahertz dalgalarının (0.1-10 THz) hızla gelişen uygulamaları, terahertz dalga algılamanın veriminin iyi anlaşılmasına ihtiyaç duymaktadır. Yoğun, koherent ve sürekli elektromanyetik dalga kaynağı, yüksek sıcaklık süperiletken (YSS) olan $Bi_2Sr_2CaCu_2O_{8+\delta}$ (Bi2212) tek kristali tarafından sağlanmaktadır. Aynı zamanda Bi2212 tek kristali uygun koşullar altında THz dalgalarının algılanmasında kullanılır. Bugünlerde, çeşitli tipteki bolometreler THz dalgalarını algılamada kullanılır. Ancak bu bolometreler, yavaş tepki zamanı ki en önemli problem ve maliyetli soğutma sistemleri gibi bazı problemsel limitlere sahiptir. Bu çalışmada, tek kristal Bi2212 istenilen kalınlığa gelene kadar scotch bant ile katmanlarına ayrıldı. Buradan sonra, safir alttaş üzerine yapıştırıldı ve kloroform ve ultrasonik titreştirici yardımıyla scotch bant çıkarıldı. Kristal üretiminden sonra tam kalınlığın bulunması için atomik kuvvet mikroskobu kullanılarak kalınlıkları tespit edildi. Daha sonra, örnekler 400^oC de 1 saat boyunca tavlandı ve arkasından ısısal buharlaştırma cihazında 150 nm altın kaplandı. Kontak direncini düşürmek için tekrar 425^oC de 30 dakika boyunca tavlandı. Temiz oda sürecinden sonra elektron demeti litografisi ile log-periyodik anten tasarımımız kristalin üzerine oluşturuldu ve Ar-iyon demeti dağlanması sayesinde son halini aldı. Son olarak dört nokta kontağı iki kontak yoluna gümüş epoksi ile alındı. a-b ekseninin sıcaklığa bağlı direnç değişiminin ölçümleri gerçekleştirildi.

To my Family

TABLE OF CONTENTS

LIST OF FIGURES

LIST OF TABLES

Table **Page**

CHAPTER 1

INTRODUCTION

1.1. Terahertz Radiation

The Terahertz (THz) region is part of the electromagnetic spectrum lying between microwaves and the far-IR. This region refers to electromagnetic radiation in the frequency interval from 0.1 to 10 THz and 1 THz corresponds to a scale of 1 ps, 300 μm as a wavelength and 4.1 meV photon energy.

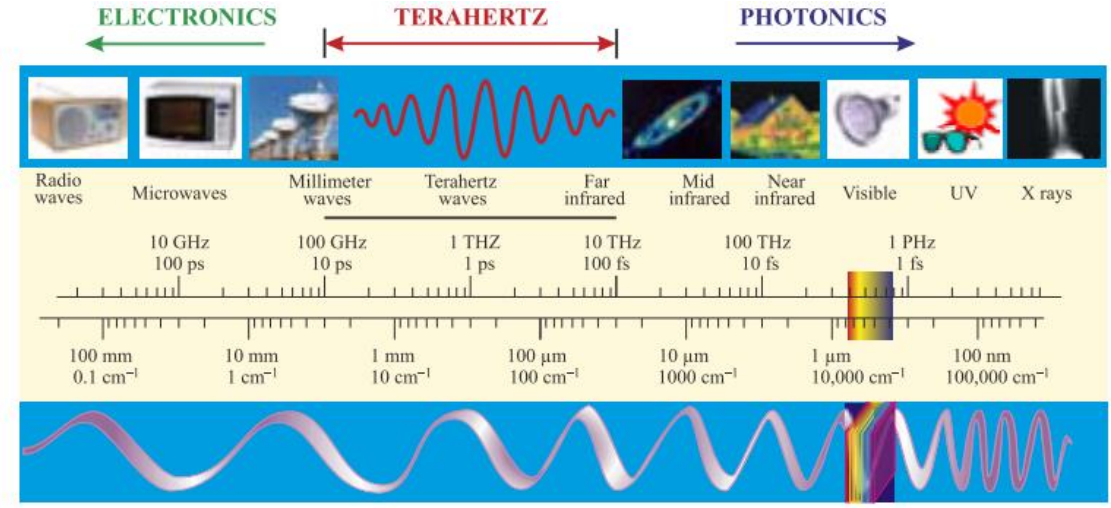

Figure 1.1. The electromagnetic spectrum with THz gap
(Source: Rogalski and Sizov, 2011)

Terahertz radiation has unique features that are not found in other parts of the electromagnetic spectrum. X–rays are energetic enough to ionize an atom by extracting an electron. But this ionization process causes damage to the human body. On the contrary, T-rays are non-ionizing radiation, like radio waves or microwaves. Hence, people exposed to T-rays will not suffer from negative effect of radiation (Kawase 2004). At the same time terahertz radiation cannot pass through metals, and is attenuated greatly through water, leather, fabric and paper (Ferguson and Zhang 2002).

The terahertz frequency range in the electromagnetic spectrum is extremely important and is the most scientifically rich band for research. In the last 20 years, scientists have discovered that organic molecules resonate in this range. This means that all organic materials can be detected by using terahertz radiation. This development has many interesting and challenging applications. Explosive materials, toxic gases and biological weapons have the potential to be detected by the presence of a hand held T-ray radar remotely (Mueller 2006). The medical community has shown that terahertz waves can detect the cancer, viruses, bacteria and other diseases instantly without surgery, biopsies, or other expensive procedures making this an important and urgent application terahertz waves (Mueller 2006). Another areas are pharmaceutical and agriculture which are using it in quality control and research. In additionally, it has great potential in ultra-high bandwidth wireless communication networks and inter-satellite communication (Tonouchi 2007). There are many techniques for generating THz radiation such as femtosecond lasers, synchrotron light, backward wave oscillators etc. But generation of THz has many problems and there is a need for powerful, low-cost, continuous wave, compact, portable room temperature, solid state terahertz sources. Some of these sources will be explained in Chapter 1.4.

1.1.1. Application Areas of Terahertz Radiation

Although THz radiation is a significant portion in the electromagnetic spectrum, researchers have difficulty in develop many applications. Nevertheless, it provides extremely attractive research fields and useful application in different fields such as medical imaging, security, scientific use and imaging, communication and manufacturing. Here, these are explained briefly.

Medical Imaging: Since T-rays are non-ionizing, it does not damage tissues and other samples, unlike more energetic X-rays. Some frequencies of THz spectrum can penetrate a few millimeters in low water content and after this it can reflect back. Also, terahertz radiation can classify a tissue which has water content and density. Hence, it is safe and less harmful for detection of epithelial cancer and can be useful for medical imaging. Since to terahertz waves have one million times weaker photon energy than X-rays, it is

safer, less invasive and painful in applications such as medical imaging. Finally, some frequencies of terahertz waves can image teeth in three dimensions (Mueller 2006).

Security: Terahertz radiation can penetrate fabrics, packing material, plastics etc., so these kind of materials can leave unique spectral fingerprints in the terahertz range. This knowledge enables imaging from spectral fingerprints. So it can be used in surveillance, such as security monitoring, to uncover concealed weapons on a person, remotely (Mueller 2006).

Scientific use and Imaging: Spectroscopy in terahertz radiation provides novel information in chemistry and biochemistry. THz time-domain spectroscopy (THz TDS) and THz tomography have been shown to be able to perform measurements on, and obtain images of, samples which are opaque in the visible and near-infrared regions of the spectrum. When the sample is very thin or has a low absorbance it can be very difficult to distinguish changes in the THz pulse caused by the sample or from those caused by long term fluctuations in the driving laser source or experiment (Pawar, et al. 2013). In addition, THz- TDS produces coherent and broadband radiation, so such images can contain much more conventional information than image formed with a single-frequency source.

In one particular instance, THz waves provides an advantage to art historians. They can see hidden historical artefacts without damaging the artwork (Jackson, et al. 2011).

Communication: Terahertz radiation have some benefits such as small antenna sizes and large information bandwidth can be achieved using terahertz carriers in secure telecommunications. THz waves can penetrate through aerosols much greater than infrared and optical wavelengths, so this signal is more useful for communications system in the stratosphere. It can be used in high-altitude communications; aircraft to satellite or above altitudes where water vapor can cause signal absorption (Fox and Bertsch 2002).

Manufacturing: Terahertz screening is used in manufacturing area as quality control and process monitoring. Also, these generally exploit the traits of plastics and cardboard being transparent to terahertz radiation, making it possible to inspect packaged goods (Mittleman, et al. 1999).

Some images about the some part of the applications of THz radiation area shown in the Figure 1.2.

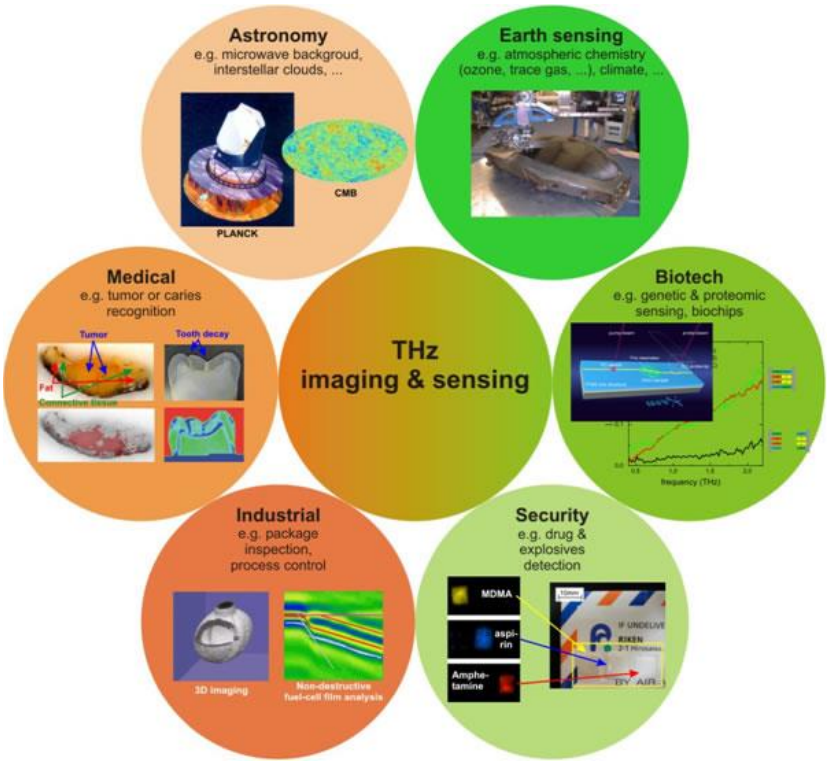

Figure 1.2. Some images of some areas of applications in THz regime
(Source: De Maagt, et al. 2005)

1.2. Terahertz Generation

Terahertz science has become increasingly popular in the recent years due largely to the advent of time-domain spectroscopy (TDS) with ultrashort pulse laser sources, which makes it possible for researchers to carry out time-resolved “far-infrared” (FIR) studies and to explore spectroscopy and imaging applications in the submillimeter wavelength regime.

Terahertz spectroscopy gained popularity in the mid-1970s (Kerecman 1973; Ashley and Palka 1973; Fleming 1974). Advanced techniques in optical rectification and photoconduction had been developed, in consequence of the efforts of many researchers and scientists (Auston 1983; Smith, et al. 1988). In 1989, terahertz- time domain

spectroscopy (THZ-TDS) was developed by Martin van Exter (van Exter, et al. 1989). Hu and Nuss in 1995 generated two dimensional (2D) images, where geometric image formation of an object was done in the T-ray frequency range. Terahertz waves were used to image opaque objects such as; the separation of cancer from normal cells (Woodward, et al. 2002), the study on pathological samples of human skin (Gladkova, et al. 2000) and detection of tooth decay in 3D (Arnone, et al. 2000).

Sources can be categorized as broadband and narrowband THz sources.

Broadband THz Sources: Photocarrier acceleration in photoconducting antennas, second-order non-linear effects in electro-optic crystals, plasma oscillations and electronic non-linear transmission lines are various sources for generating terahertz radiation (Ferguson and Zhang 2002). On the other hand, these all sources that have very low conversion efficiency. Hence, average THz beam powers are in the range of nano to microwatt range. While the average power of the femtosecond optical sources is in the region of 1 W.

Photoconduction and optical rectification are most commonly used techniques for generation of broadband-pulsed terahertz radiation. GaAs, InAs and radiation damaged silicon wafers have very high resistivity and a photoconductor can be patterned on them. This generation is based on an ultrafast laser pulse which creates electron-hole pairs in the photoconductor. Optical rectification is (OR) based on the inverse process of the electro-optic effect and it is a second-order nonlinear effect, whereby an ultrafast electric field pulse is rectified in a χ^2 medium in this case an electrooptic (EO) crystal. The ultrafast pump pulse induces a transient polarization, $p(t)$ which in turn emits a T-ray bandwidth pulse. The time evolution of the T-ray pulse is given by the second time derivative of the polarization transient, $E_{THz}(t) \sim \frac{\partial^2 p(t)}{\partial^2 (t)}$. Femtosecond laser pulses are required in these techniques.

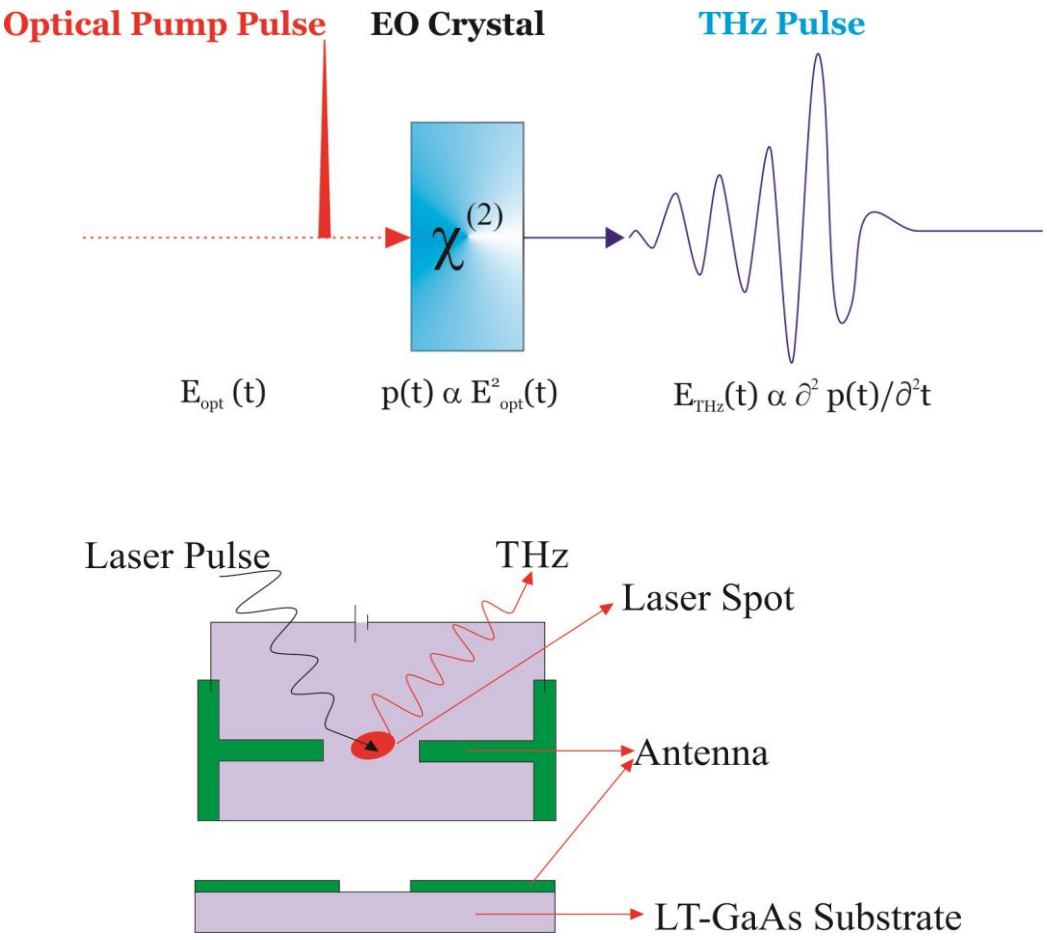

Figure 1.3. Typical schemes of optical rectification and photoconductive generation (Source: Zhang, et al. 1992; Krishna, et al. 2012, respectively)

Narrowband THz Sources: Without requesting bulky and expensive femtosecond lasers, photomixing offers an alternative method for generating terahertz radiation. Photomixing can be achieved using two CW lasers, and interference produced between two CW lasers (Brown, et al. 1993) contains different above-band gap wavelengths. In these all-photoconductive systems, inexpensive, compact, and tunable diode lasers (Gregory, et al. 2004) can be used as the laser sources.

The photomixing techniques based on CW-THz emitters and detectors mainly consist of a photoconductor and an antenna. The photoconductor can be viewed as a combination of a photoconductive switch (semiconductor) and a photomixer. The electrodes and photoconductive gap are generically termed the photomixer. The electrodes are designed as the structure of interdigitated fingers coupled to a photoconductive gap. A schematic of a typical CW-THz device is shown in Figure 1.4.

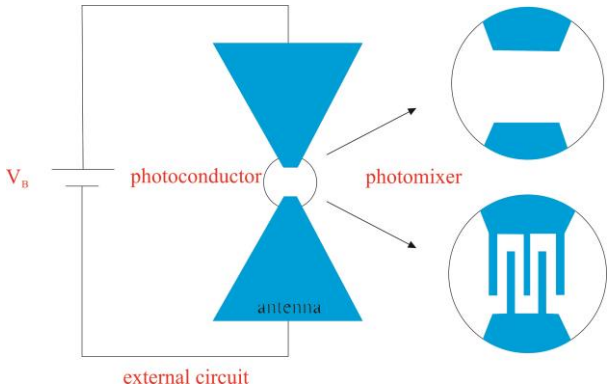

Figure 1.4. A schematic of a typical CW-THz device
(Source: Gregory, et al. 2005)

Terahertz free electron lasers (FELs) have many advantages like high intensity, combined with short pulse length, easy tunability and variable pulse structure. These properties are essential for their use in biological and medical studies (Grosse 2002) and for the exploration of vibrational and configurational molecular transitions (Kato, et al. 2000; Xie, et al. 2002) in terahertz regime. Working Principle of FELs are based on using a beam of high-velocity bunches of electrons propagating in a vacuum through a strong, spatially varying magnetic field. Schematic and setup images of the FEL show in the Figure 1.5 and Figure 1.6.

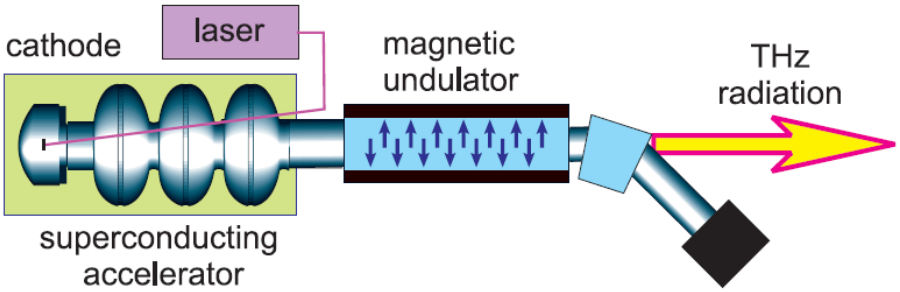

Figure 1.5. Shows a schematic terahertz FEL
(Source: Grosse 2002)

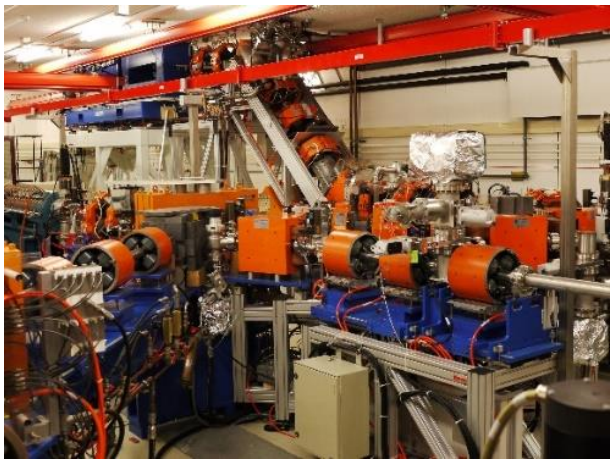

Figure 1.6. Setup in FOM Institute for Plasma Physics, Netherlands

The first terahertz quantum cascade lasers (QCLs) was demonstrated at a wavelength of 4 μm (75 THz) at Bell Labs in 1994 (Faist, et al. 2004). QCLs are based on a serial connection of coupled quantum wells which are constructed by molecular beam epitaxy (MBE) technique. QCLs have coupled quantum wells (Figure 1.7) with choice of the layer thickness of GaAs, sandwiched between potential barriers of $Al_xGa_{1-x}As$.

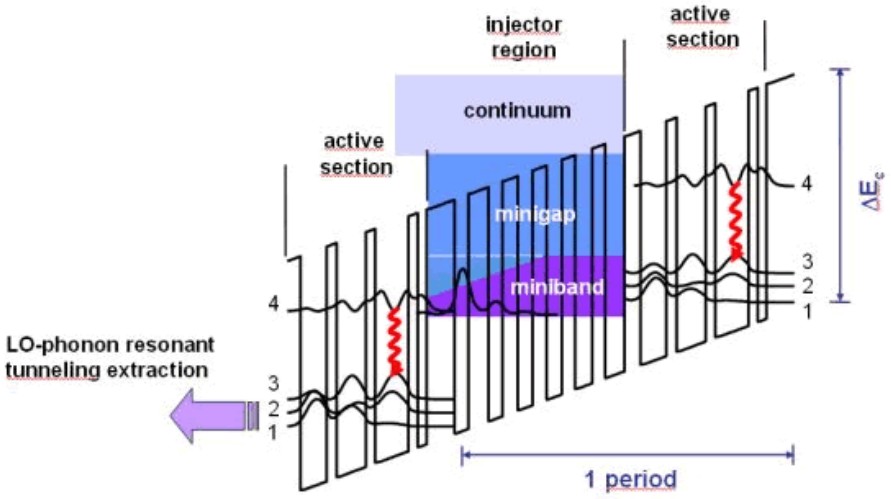

Figure 1.7. Conduction band structure of THz quantum cascade lasers
(Source: Classical Concepts of Quantum Cascade Lasers, 2013)

There is one injector and one active region. Upon population inversion electron transition to lower level occurs and this generates waves at a specific wavelength in the active region. The electrons tunnel between the quantum well and then the injector region provides coupling of them to the higher level in the active region of the subsequent repeat units. The quantum cascade lasers can be used for generating terahertz radiation in the infrared region. But generating long wavelength of terahertz radiation with these lasers are still a very significant problem.

All terahertz sources have their own disadvantages. Therefore, there is a great effort to find high power, low cost and tunable terahertz sources. There is a new approach; investigate high temperature superconductors (HTS) for terahertz science. The reason for using HTSs in generation of THz radiation is their layer by layer structure which makes possible the propagation of electromagnetic waves by Josephson plasma oscillations and this oscillations' frequency lies in the THz regime (Tachiki, et al. 1994). $Bi_2Sr_2CaCu_2O_x$ (Bi2212) single crystal is one of the most promising high temperature superconductors for THz radiation. After many studies, Ozyuzer et al. accomplished a scientific breakthrough when they obtained continuous, monochromatic and coherent electromagnetic terahertz radiation from rectangular mesa-shaped sample of the HTS Bi2212 (Ozyuzer, et al. 2007).

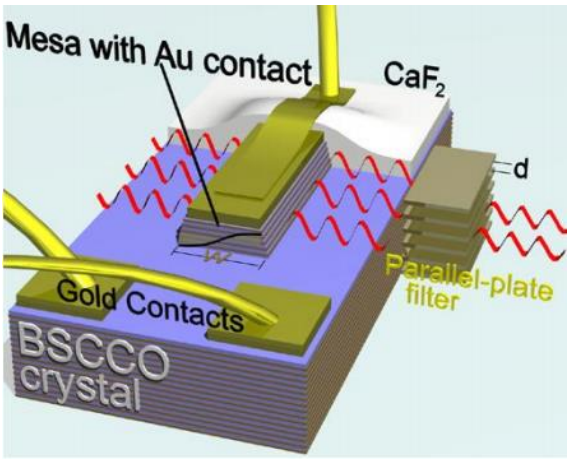

Figure 1.8. Schematic of mesa from Bi2212 crystal for terahertz emission
(Source: Ozyuzer, et al. 2007)

1.3. Terahertz Detection

Terahertz detection technology is as important as generation of THz radiation. Terahertz detectors can be categorized based on coherent and incoherent techniques. Coherent techniques measure the amplitude and phase of the field and rely on ultrafast sources, incoherent techniques measures only intensity and is typically based on thermal absorption. Now, terahertz detectors will be introduced briefly.

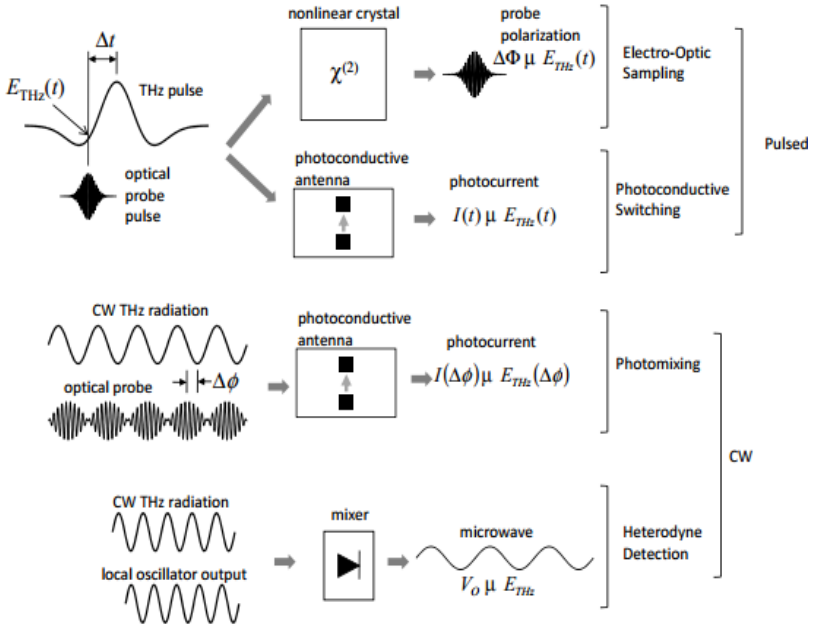

Figure 1.9. Coherent detection of terahertz radiation
(Source: Principles of Terahertz Science and Technology)

Generally, electro-optic sampling (EOS), photoconductive switching, photomixing and heterodyne detection are the most common used techniques for coherent detection of terahertz radiation. By free electro-optic sampling, the actual electric field of broadband terahertz pulses are measured by using Pockels effect. A THz field causes birefringence in nonlinear optical crystal which is proportional to field amplitude. Also, photoconductive (PC) antenna can measure the broadband pulse in the time domain. When there is no bias field, an optical probe pulse injects photocarriers and then a THz field induces a current in the photoconductive gap. The induced photocurrent is

proportional to the THz field amplitude. Another method of measuring broadband terahertz pulses in the time domain is detecting with photomixing. This technique based on exploiting photoconductive switching. So, between the optical beat and THz radiation, the photocurrent displays sinusoidal dependence on the relative phase. Heterodyne detection is based on frequency downconversion in a nonlinear device, which is named mixer, accomplished by mixing signal with reference radiation at a fixed frequency. Mostly, Schottky diodes are used as a mixer. The mixer produces an output signal at the difference frequency called the "intermediate frequency" which is proportional to amplitude of THz. Heterodyne detection technique is generally used to detect CW incoherent terahertz radiation as different from the optical techniques. There are two generalized parameters when characterizing THz detectors. One of them, Noise Equivalent Power (NEP) which is described as the incident RMS optical power required in order to obtain signal-to-noise ratio of 1 in a bandwidth of 1 Hz and NEP is related to the minimum power that the photodetector can detect,

$$NEP = < i_n^2 > / R \tag{1.1}$$

where i_n is the noise current, and R is the detector responsivity. Other one is the detectivity which can defined as

$$D^* = \sqrt{SB/NEP} \tag{1.2}$$

where B is the bandwidth and S is the detector area (Sizov and Rogalski 2010)

Golay cell, pyroelectric device and bolometers, which are incoherent detector types for detection of THz radiation, are most commonly used thermal sensors. Generally, all devices have a thermometer that is used to measure the temperature difference in the absorber and a radiation absorber attached to a heat sink. All thermal detectors are classified by its specific configuration and scheme which are used to measure the temperature difference.

Golay cell was invented by Marcel J. E. Golay, after whom it came to be named, in 1947. It can sense radiation which has radiation power levels down to 10 μW at THz

frequency. A Golay cell detector, which is a room temperature detector, works based on the differences in volume or pressure (thermal expansion) of an encapsulated gas with temperature. The schematic and device representation of Golay cell can be seen below in Figure 1.10.

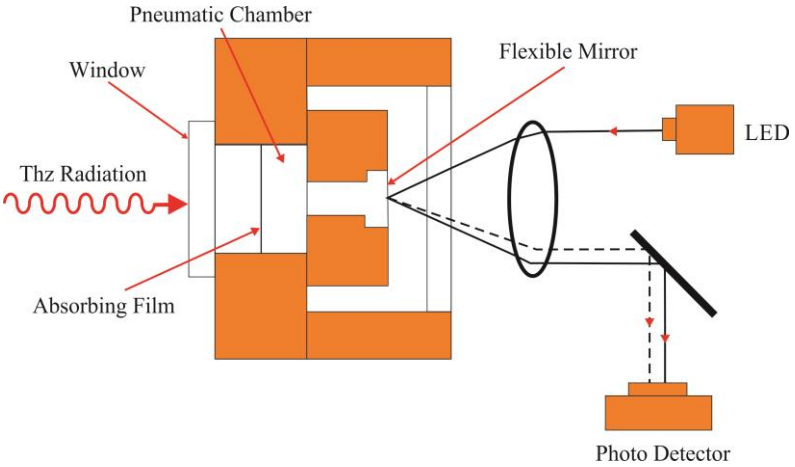

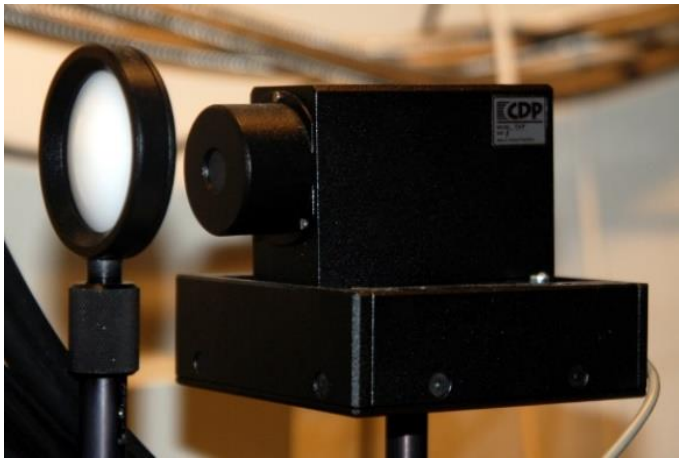

Figure 1.10. The schematic (Source: Principles of Terahertz Science and Technology) and device of Golay cell (Source: Golay Cell, 2014)

Basically, incident THz radiation reaches the front window and then passes it. After that, electromagnetic radiation is absorbed by absorbing film. This absorbed energy induces thermal expansion of the gas. The result of pressure rise deforms the flexible mirror attached to the backside of the chamber. An optical beam from a light emitting diode is focused on the flexible mirror, which reflects the beam onto the photodetector.

The Golay cell is the most sensitive detector among thermal detectors which operates from 20 GHz to 20 THz spectral range and typically obtained NEP is $1^{-10}W.Hz^{-1/2}$.

Terahertz applications that do not need high sensitivity typically can use pyroelectric detectors (Figure 1.11). Triglycine sulfate (TGS) and Lithium Tantalate ($LiTaO_3$), which are pyroelectric materials, show a large spontaneous electrical polarization which varies with temperature and this physical phenomenon is called pyroelectricity. These detectors have some properties such as; they can only sense AC signals, operate at room temperature and have a small size which can give fast thermal response time <1 μs (REF). The cut-off wavelength of unstressed detectors is 120 μm. However, if applying the stress to the crystal, it can be extended to 200 μm. The performance of pyroelectric detectors depend on the operating condition. It has 1 $nWHz^{-1/2}$ NEP in the low radiation background conditions and response speed is limited, perhaps to 20 Hz (-3 dB). In higher background laboratory applications operates at 50 kHz (-3 dB) with much reduced sensitivity.

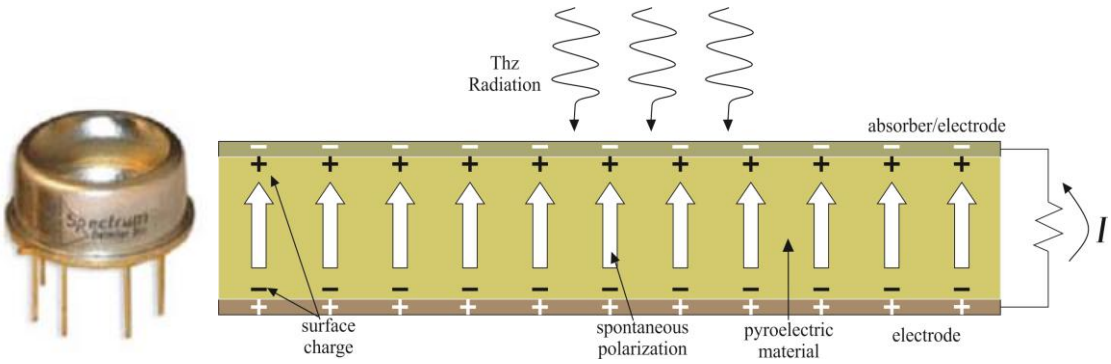

Figure 1.11. Schematic diagram and device of a typical pyroelectric detector (Source: Principles of Terahertz Science and Technology)

A bolometer, was invented by Samuel Pierpont Langley in 1878, is a thermal detector where the electrical resistance of the material is the property that is measured in response to incident electromagnetic radiation in a wide spectral range from THz to X-rays. If a bolometer consists of a number of components, it is called composite bolometers which show better performance because each function of components can be optimized separately. The device consist of a thermometer whose electrical resistance varies according to the substrate temperature. The substrate is connected to a heat sink which

includes a L-He Dewar to keep the detector at cryogenic temperature in order to acquire high detection sensitivity. Radiation energy absorbed by the absorber is converted into heat, which raises the temperature of the absorber and thermometer assembly. The temperature increase induces a change in the thermometer resistance, which is detected by measuring the change of the electrical signal across it. The structure of a bolometer detector can be seen in Figure 1.12.

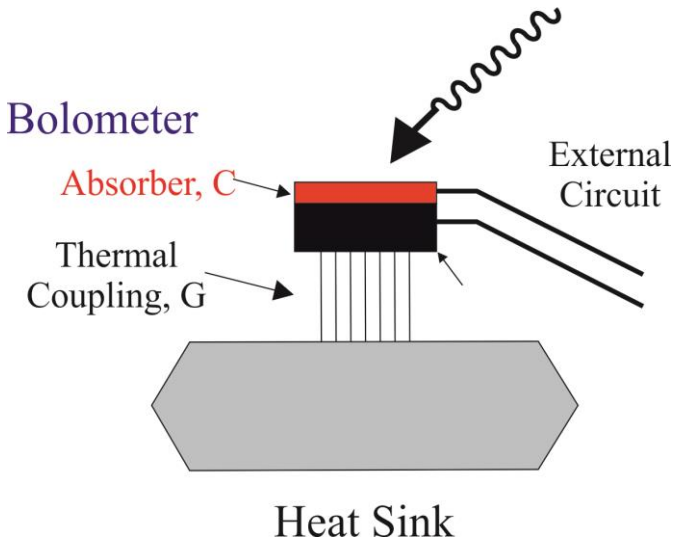

Figure 1.12. Schematic design of a Bolometer
(Source: Van Neste, et al. 2008)

The thermistor can supply the direct thermal contact with the film and have reduced thermal capacitance. This enables a shorter thermal time constant. Typical Si bolometer has $\sim 10^7\ V/W$ responsivity at L-He temperature. Its noise equivalent power (NEP) is $\sim 10^{-14}\ W.Hz^{-1/2}$. Low reflectivity and high absorptivity are the quantities of a radiation absorber of good quality higher efficiency. The substrate prefers high thermal conductivity and low heat capacity. For highly efficient, absorber/substrate assembly contains a thin metal film deposited on a thin crystalline dielectric substrate such as bismuth (Bi) diamond and sapphire. Bi is widely used for the absorber material because of the Bi has low conductivity, high absorptivity and very small capacity. Also, Bi film is relatively thick, it is easy to keep the film thickness uniform. Another material, diamond is the best material because of its perfect thermal conductivity and high transparency in the THz region below 30 THz. Sapphire also has a very good thermal conductivity, and

is transparent below 10 THz. The thermometer must have low heat capacity and electrical noise and it is thermally attached to the absorber/substrate assembly. The most widely used materials for the thermometer are heavily doped Si and Ge. In order to maximize detection sensitivity, the absorber area needs to be minimized. In other words, when all parts of bolometer are adjusted to optimum parameters, maximum detection sensitivity can be achieved.

1.4. Superconductivity

The phenomenon of superconductivity was discovered by H. Kamerlingh Onnes (Onnes 1911) who studied on the temperature dependence of the resistance of a sample of mercury at low temperatures. The mercury undergoes a phase transition from normal state to a superconducting state with no electrical resistance which is not very small but is exactly zero at temperatures below the temperature of 4.2 K. Thus, any small electrical current which may occur in the superconducting sample will not decay and persists as long as the sample temperature is kept below T_c. In this way, perfect conductivity is the first important property of superconductivity.

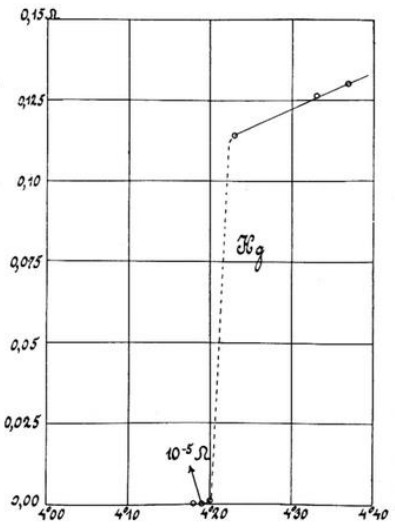

Figure 1.13. The first introduce of superconductivity
(Source: Onnes 1911)

Many metals (Sn, In, Al and others) were found to have superconducting properties after the discovery of superconductivity in mercury. Only pure metals of Nb and Pb have highest T_c about 9.2 K and 7.2 K, respectively.

The second important property of superconductivity is perfect diamagnetism, which is known as Meissner Effect (Meissner and Ochsenfeld 1933) (Figure 1.14).

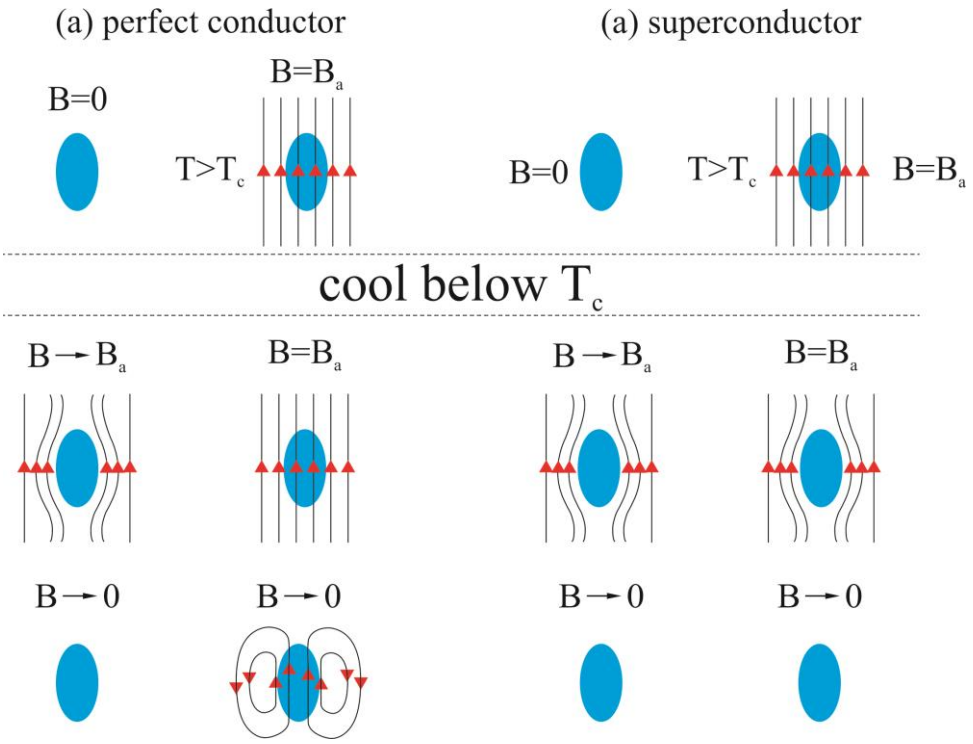

Figure 1.14. Meissner effect
(Source: Superconductivity, 2009)

In 1933, Meissner and Ochsenfeld showed that in magnetic fields below a certain threshold value the flux inside the superconductor material was averted. It is known from the Maxwell's equations that it will not allow a magnetic field to enter the region if the material has zero resistance. In the 1950's it was determined that superconducting materials can be separated into two categories exhibiting different behavior, Type I and Type II superconductors. A Type I superconductors obey Meissner effect but Type II superconductors have two critical magnetic fields H_{c1} and H_{c2} which are dependent on temperature. Under the first critical magnetic field values (H_{c1}) it expels magnetic field. Between the H_{c1} and H_{c2} magnetic fields, material remains a perfect conductor. In the

mixed state, also called vortex state, the magnetic field penetrates into superconductor in quantized units of magnetic flux. Thus, in the mixed state there are normal regions surrounded by superconducting regions (Figure 1.15).

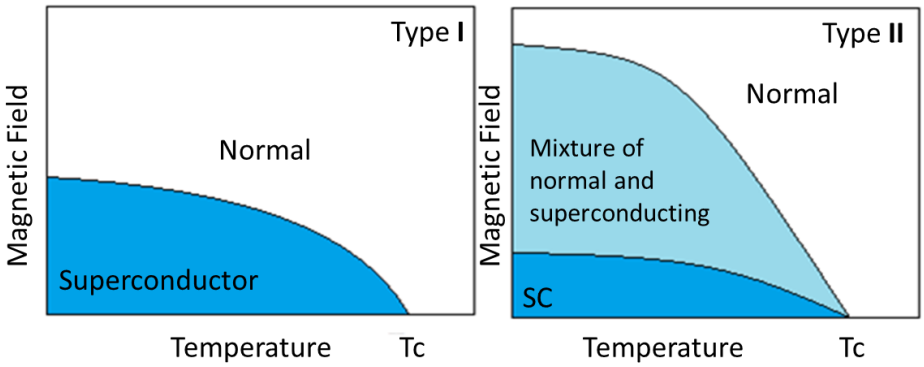

Figure 1.15. Type 1 and Type 2 superconductors

Another theory was put by Landau and Ginzburg in 1950. This theory explained many properties of superconductivity and combined the Landau's theory of second order phase transitions with Schrödinger-like wave equation. Abrikosov showed the two types of superconductors and state of vortex can only be found in the Type II superconductors.

H. Frönlinch proved the transition temperature would decrease as long as the average isotopic mass increased which is known as isotope effect and was observed experimentally in 1950 by Maxwell, Reynolds et al. The relationship between the critical temperature and the isotope mass $\frac{M}{T_c M^{\frac{1}{2}}} = constant$ was found by studying on different superconducting isotopes of mercury. This effect caused the electron-phonon interaction system of superconductivity. And isotope effect lead to improvement of BCS theory of superconductivity.

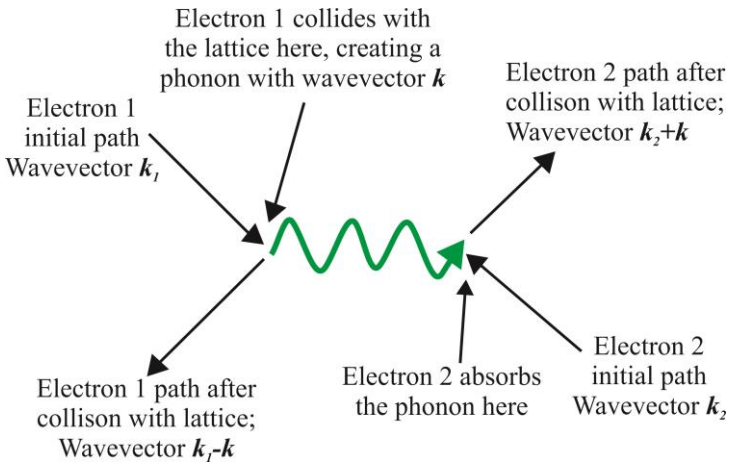

Figure 1.16. A model of Cooper pair attraction
(Source: Background Physics, 2006)

The microscopic theory of superconducting was formulated by Bardeen, Cooper and Schrieffer in 1957. According to BCS theory, derived from the first letter of each person's last name which was awarded the Nobel Prize in 1972, conduction electrons form pairs which have opposite spin and momentum, known as Cooper pairs. These pairs have zero spin and hence obey Bose-Einstein statistics. At low temperature, all pairs are separated by a gap Δ that is related to the binding energy of the Cooper pairs. The results of Ginzburg-Landau (1950) and London (1950) were confirmed with BCS theory. Experimentally, the energy gap changes with temperature as was shown in the BCS theory. When T=0, the ratio of $2\Delta(0)/k_bT_c$ is between 3.2 and 4.6 in superconductor elements and the ratio predicted by BCS theory is equal to 3.5 (Wesche 1998).

When the temperature is close to transition temperature, BCS was converted to Ginzburg-Landau theory, in 1959 by Gor'kov (Gor'kov 1960). This theory becomes important. Because it is explains the Ginzburg-Landau validity and enables simpler calculation than BCS theory.

Tunnelling was discovered in 1960's. Giaever did experiment on superconducting tunnelling system (Giaever 1960). After a few years, Josephson explained the tunnelling of superconductors theoretically (Josephson 1962).

1.5. High Temperature Superconductors

Many years of research on numerous superconducting alloys and compounds had been discovered after the Kamerling Onnes discovery with the highest T_c being 23.2 K. K. Alex Müller and J. Georg Bednorz discovered superconductivity in copper-oxide based compounds and this discovery led them to receive Nobel Prize in 1987. Their mixture was consisting of lanthanum, barium, copper and oxygen ($La_{2x}Ba_xCuO_4$) and has 35 K transition temperature (Bednorz and Müller 1986). Some scientists produced the lanthanum compounds which has 40 K at ambient pressure and about 52 K under high pressure (Chu, et al. 1987). A remarkable evolution came in 1987 with the discovery of high temperature superconducting in the complex oxide $YBa_2Cu_3O_7$ by replacing La^{3+} with Y^{3-} which has a transition temperature about 92 K (Wu, et al. 1987). The importance of this discovery is based on the fact that the superconductors could then be cooled with liquid nitrogen (77 K) which is much cheaper and has more commercial applications in superconductivity area than liquid helium. Just a year later in 1988, two superconducting phases characterized as $Bi_2Sr_2CaCu_2O_{8+\delta}$ (Bi2212) and $Bi_2Sr_2Ca_2Cu_2O_{10+\delta}$ (Bi2223) were discovered with their T_c 95 K and 110 K, respectively (Maeda, et al. 1988). In the same year, the critical temperature reached at 125 K with the discovery of $Tl_2Ba_2Ca_2Cu_2O_\delta$ (Tl2223) (Hazen, et al. 1988). Finally, to date the record at ambient pressure stands at 135 K in Hg based cuprates $HgBa_2Ca_2Cu_3O_{8+\delta}$ (Hg1223) superconductor compound (Schilling, et al. 1993) and the transition temperature of this compound can reach up to 165 K at high pressure (Gao, et al. 1994). Figure 1.17 shows the superconducting critical temperature of several cuprates as a function of the year of discovery, as well as T_c of some metallic superconductors.

Nagamatsu and friends discovered the new material MgB_2 with T_c 39 K in 2001 (Nagamatsu, et al. 2001). MgB_2 superconductors obey conventional models of superconductivity and has relatively basic structure if compared with the cuprates. In 2006, new compound was discovered LaOFeP. But it did not receive much attention because of its transition temperature was very low (Kamihara, et al. 2006). Fe-doped LaOFeAs was found to be superconductor at 43 K (Takahashi, et al. 2008) and iron-based oxyarsenide $Sm[O_{1-x}F_x]FeAs$ with the critical temperature 55 K was discovered (Ren, et al. 2008).

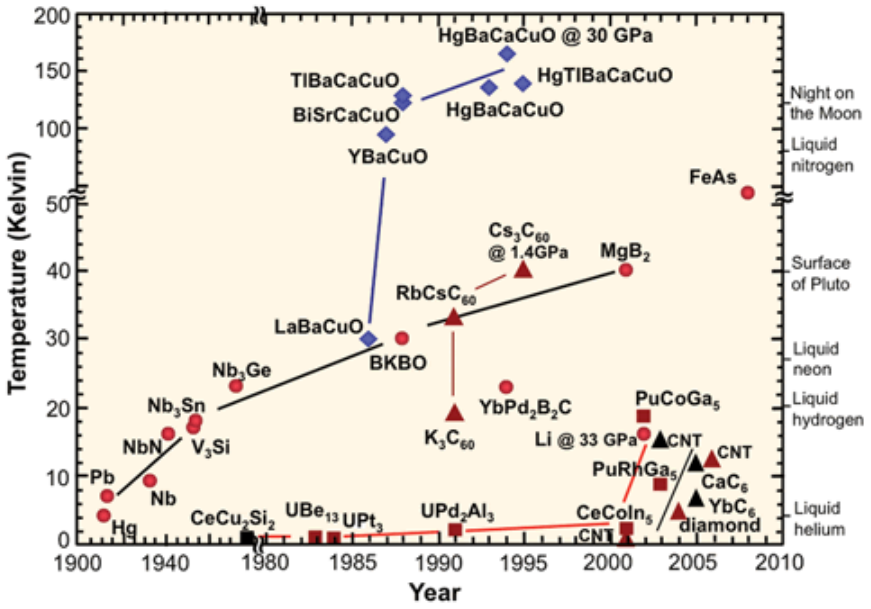

Figure 1.17. The timeline of discovery of superconducting materials
(Source: Image courtesy of Department of Energy - Basic Energy Sciences)

All known high temperature superconductors are Type II superconductors. Type I superconductors expel all magnetic fields due to Meissner Effect. However, Type II superconductors allow magnetic fields to penetrate their interior in quantized units of flux and they can used for magnet and energy applications which can be well defined by the Ginzburg-Landau theory (Landau and Ginzburg 1950).

Type I and Type II superconductors have some different points such as critical fields, London penetration depth λ and coherence length ξ. If a superconductor's coherence length is bigger than London penetration depth ($\xi>\lambda$), it shows that it has the characteristics of Type I superconductors, but as the situation is $\xi<\lambda$, it has the characteristics of Type II superconductors. Moreover, if the ratio λ/ξ called the Ginzburg-Landau parameter (κ) is greater than $1/\sqrt{2}$, superconductor must be type II (Wesche 1998). Although the values of the coherence length ξ of HTSs are short, they have large critical magnetic field.

1.6. Objective of the Work

An unexplored part of the electromagnetic spectrum, the terahertz (THz) region (0.3 - 10 THz), has ever-increasing importance. The reason for this, is the possibility of being used in so many different areas such as from defence and security to the health sector. Practically terahertz waves can be used for imaging (for example Golay cell and pyroelectric detector). But these detectors have generally high time constants (> 30 ms) and low sensitivity. Sensitive bolometers, which have NEP $10^{-13} W/\sqrt{Hz}$, are not practical due to their time constant being greater than 5 ms and their use of liquid helium. THz wave imaging with high temperature superconductor crystal $Bi_2Sr_2CaCu_2O_{8+d}$, which has critical temperature $T_c = 70\ K$, reduce working temperature to around 77 K so cooling is possible with liquid nitrogen.

In this project, a bolometer chip is designed to be cooled by liquid nitrogen without liquid helium, and with high critical temperature. It will be used for imaging and the characteristic time is sufficiently small. Developed bolometer chip will have antenna for detecting THz waves between 0.3-10 THz and the sensitivity will be increased with the filter structures and THz absorbing coating. Bolometer chip is placed in a designed cryostat, electronics and software of the system have small size and is ready to use.

CHAPTER 2

BOLOMETERS

2.1. Principle of Bolometers Operations

Bolometers measure the power of the radiation through absorption and a thus resulting change in resistance is induced by absorption of radiation and the resulting current/voltage change is measured. This change is proportional to the absorbed power.

Many detectors can be used in the optical and far-infrared ranges. But in the THz regime, these detectors show only weak performance. The bolometer principle was developed at the end of the 19^{th} century by S. P. Langley in 1878 (Langley 1881) as a tool to measure the infrared spectrum of the sun. He used a setup where two identical thin platinum stripes covered with carbon black lay close to each other. Only one of them was irradiated by light and warmed up. This heating caused the change in resistance which was measured with a Wheatstone bridge (Langley 1898). The most important parameters are sensitivity and speed of the bolometer.

Bolometers use in detectivity of thermal radiation without any change on basic setup since their developments. The basic components of the bolometer is shown in Figure 2.1.

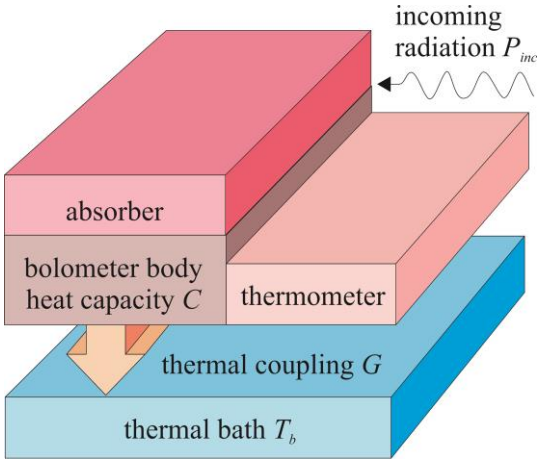

Figure 2.1. Schematic of a classical bolometer which consists of three basic parts. An absorber, the bolometer body with a heat capacity C and a thermometer. The bolometer isothermally coupled to a thermal bath with temperature T_b. The thermal coupling is described by the thermal coupling coefficient G (Source: Stockhausen 2013)

The bolometers have some special parts. One of them is absorber material that converts the incoming radiation P_{inc} into heat. When the radiation absorbed by the absorber material, it produces heat which is transferred to the bolometer body. The bolometer body heats up depending on the amount of power absorbed by its heat capacity, *C*. A thermometer measures the temperature change in the bolometer body. The temperature difference between the irradiated and non-irradiated states is directly proportional to the power of the absorbed radiation. When the bolometer body is coupled to thermal bath, it returns to its initial state. The thermal coupling is described by the thermal coefficient, *G*. The thermal coefficient manages the time in which the absorbing heat can leave the bolometer body. If the absorber of the bolometer is not enough irradiated, the temperature of the bolometer body T relaxes back to the temperature of the thermal bath T_b. The time dependence of a bolometer can be described according to (Richards 1994) using the thermal balance equation of the system:

$$P_{inc} = G(T - T_b) + C\frac{dT}{dt} \tag{2.1}$$

The speed of this temperature change or its inverse, the time in which the bolometer can relax to its equilibrium state is defined by:

$$\tau = \frac{C}{G} \tag{2.2}$$

Also, this time constant can be derived from equation (2.1).

If the bolometer body has a large heat capacity, C, it can store more heat than a bolometer with a small heat capacity. If the bolometer has a small heat capacity, it will relax much faster to the bath temperature than the bolometer with the large one for a fixed thermal coupling. The thermal coupling coefficient defines how fast the heat can be transferred from the bolometer body to the thermal bath. The bolometer with larger thermal coupling coefficient the faster relaxation back into the initial state.

If a bolometer is irradiated by a radiation source with an amplitude modulated output power the temperature change of the bolometer depends on the modulation of the incoming radiation.

$$P_{inc}(t) = P_o + \Delta P(wt) \tag{2.3}$$

where w is the modulation frequency of the output power. When the equations (2.1) and (2.3) are combined, the temperature response of the bolometer ΔT on the incoming radiation power ΔP can be calculated according to (Richards 1994)

$$\frac{\Delta T}{\Delta P} = \frac{1}{G\sqrt{1+w^2\tau^2}} \tag{2.4}$$

where τ is the time constant from (2.2). Equation (2.4) describes the thermal sensitivity S_{th} of the bolometer to incoming radiation in [K/W]. The magnitude of the thermal sensitivity depends on the thermal coupling coefficient (G) and τ on the heat capacity of the bolometer body. The modulation frequency w of the incoming radiation is affected by two factors. In the limit of ($w.\tau >> 1$) equation (2.4) simplifies to

$$\frac{\Delta T}{\Delta P} = \frac{1}{Cw} \tag{2.5}$$

The response time of bolometer is proportional to the inverse of its heat capacity. An increase of the modulation frequency leads to a reduction in sensitivity. For high sensitivities in this mode of operation the heat capacity has to be as small as possible. In the limit of ($w.\tau << 1$) equation (2.4) simplifies to

$$\frac{\Delta T}{\Delta P} = \frac{1}{G} \tag{2.6}$$

The response increases with a reduction of the thermal coupling but the time constant of the bolometer increases. The factor G should be selected as small as possible for optimum performance. The sensitivity and the speed of the bolometer is constant.

$$S_{th}\tau^{-1} = const. \propto C \tag{2.7}$$

There is only one way to increase the temperature response of a bolometer without changing the speed is by variation of the heat capacity of the bolometer body. The heat capacity can be calculated from the volumetric heat capacity C_v of the bolometer material and the volume of the bolometer body V to $C = C_v V$. The volumetric heat capacity depends on the material choice for the bolometer body.

The power of the incoming radiation can change the temperature response of the bolometer. A thermometer has to be used to measure this temperature change. There are different thermometers and depending on the type of thermometer, the response of the bolometer can be measured using different quantities. The most common form of bolometer is the resistive bolometer. The temperature is measured via a resistor that has well known temperature dependency *R (T)* in this type of bolometer.

The signal response is proportional to the change of incoming radiation power when biasing a resistive bolometer with a constant current I_b. It can be measured by using the voltage change due to the heating of the resistor with constant bias current

$$\Delta V = I_{bias}.\Delta R \tag{2.8}$$

The electrical sensitivity *S* of such a resistive bolometer is defined as the change of the detector voltage ΔV over the change of radiation power ΔP. Taking equation (2.8) and (2.4) the sensitivity can be written as

$$S = \frac{\Delta V}{\Delta P} = I_{bias} \cdot \frac{\Delta R}{\Delta T} \cdot \frac{1}{G} \cdot \frac{1}{G\sqrt{1+w^2\tau^2}} \tag{2.9}$$

The thermal sensitivity of the bolometer and the electrical sensitivity of the resistive bolometer have same form and thus same dependencies concerning *C*, *G* and τ apply. Also, equation (2.7) remains same $S\tau^{-1} = const. \propto C$. This means that the sensitivity of the bolometer can still only be increased at the supply of the speed.

The resistive thermometer knows to increase the sensitivity of the bolometer without decreasing its speed. The sensitivity of a resistive bolometer directly depends on the steepness of the temperature derivative of the resistance which is a property of the material the thermometer is made of.

The choice of material for different parts of the bolometer is of great importance for the optimization of the sensitivity and the speed of the bolometer. The absorber should be made from a material that can absorb maximum incoming radiation. Also, the temperature derivative of resistance $\frac{\Delta R}{\Delta T}$ of the thermometer should be as large as possible. However, the heat capacity of the bolometer should be as small as possible. And the thermal coupling of the bolometer body to the thermal bath *G* should as small as. When suitable materials are use, the bolometer can be fast and sensitive. Mostly thin metal films or semiconductors are used for bolometers operated at room temperature. Specific heat capacities of metals such as platinum $C_{p,pt} = 0.13 \frac{J}{\rho}.K$ and semiconductors such as silicon $C_{p,si} = 0.75 \frac{J}{\rho}.K$ are in the same order of magnitude. So no great difference in operation should arise from this given the volume of the bolometer is similar. Commonly used materials (Table 2.1) with a high temperature coefficient of the resistance ($TCR = \frac{1}{R}.\frac{\Delta R}{\Delta T}$) are VaO_x, SiGe and YBaCuO which range from 2 to 4 $\%/K$). Metals have a maximum TCR of 0.3 $\%/K$ in the state of the art semiconducting bolometers.

Table 2.1. TCR of various materials and techniques suitable for fabrication of uncooled bolometers (Source: Subrahmanyam, et al. 2008)

Technique	**Material**	**TCR [K^{-1}]**
Sputtering	YBaCuO	2.9-3.5
CVD	Si_xGe_{1-x}	2.4
DC Sputtering + Oxidation	VO_x	2.0
PLD	VO_x	2.8
Ion beam sputtering + Oxidation	VO_2	2.6
RF sputtering	$V_2O_5/V/V_2O_5$	2.6
RF sputtering	V-W-O	2.7-4.1
DC magnetron sputtering + Annealing	VO_2	4.4
Reactive E-beam Evaporation	VO_2+ V_2O_5	3.2

The thermal coupling between the bolometer body and the thermal bath is the only available parameter to improve the sensitivity of a bolometer at room temperature. Higher sensitivities can be achieved by increasing *G*. Placing the bolometer on a thin membrane (Torres, et al. 2003) or using a spider-web approach (Bock 1995) structure, achieved higher sensitivities. Another way to getting high sensitivities in the order of 10^6 V/W is by using the strong thermal coupling. But this way causes an increase in response times of the bolometers to several milliseconds. Materials with higher TCR at room temperature are available but they are difficult to use as bolometers.

To reduce the temperature dependent noise contributions it is common to cool down the bolometer. The strong decrease of the heat capacity of the bolometer material with decreasing temperature is another positive side effect of the low temperature operation. According to the Debye model, the phonon heat capacity of solid material at temperatures far below the Debye temperature strongly depends on the temperature $C_v \propto T^3$ where C_v is the volumetric heat capacity of the material. Therefore, the speed of the bolometers significantly increases at low temperatures.

2.1.1. Superconductor Bolometers

Superconducting materials become possible applicants as material for the bolometer body when operating at low temperatures. They show a strong dependence of their resistance on the temperature at their superconducting transition temperature T_c. Figure 2.2 shows superconducting transition from a thin tantalum wire bolometer (Andrews, et al. 1942). Superconducting bolometers made from titanium have shown transition widths in the range of a few mK (Lee, et al. 1998).

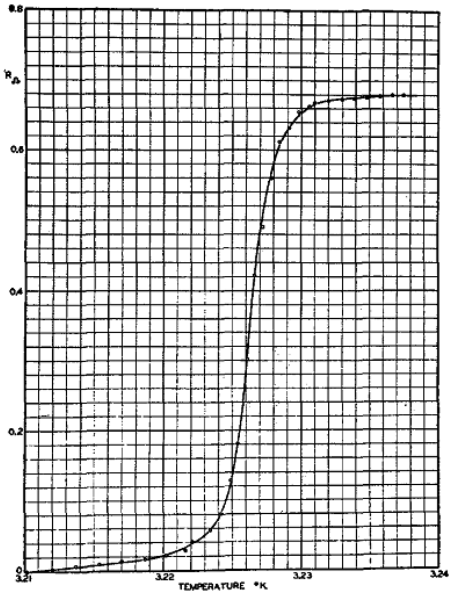

Figure 2.2. The resistance over temperature behaviour of a thin superconducting tantalum wire close to its critical temperature T_C is shown (Source: Lee, et al. 1998)

The TCR of a superconductor operated on its transition can be orders of magnitude higher than for conventional semiconductor or normal metal bolometers due to the very small width of their superconducting transition ΔT_c. Thus, they are very well suited as thermometers (Irwin 1995) for bolometers. A common approach to take advantage of these properties is to use composite superconducting bolometers with a non-superconducting absorber and a small superconducting bolometer body a thermometer (Anders, et al. 2009). Bolometers with a superconducting thermometer have to be operated at temperatures below or close to T_c. Detectors operated on the superconducting

transition direct detection mode are called transition-edge sensor (TES). This type of detectors have been supplied to be very sensitive with noise equivalent power of $NEP = 5.10^{-17} \frac{W}{\sqrt{Hz}}$ for titanium detectors at 375 mK and also they have 13 ms response time.

When reduce the bolometer dimensions, heat capacity of the bolometer body is also reduced. Then the speed of the bolometer is increased. The heat capacity of the bolometer directly depends on its volume such as $C = C_v.V = C_v.w.l.d$ where w is width, l is length and d is thickness of the bolometer. Therefore, a detector which has minimum dimensions, is preferred.

For the fabrication of fast and sensitive bolometers it can be concluded that the materials used for the thermometer/bolometer body need to have highest TCR at the operation temperature.

2.1.2. Hot-Electron Bolometers (HEB)

The signal power of many interesting applications in the THz frequency range is very small which makes it difficult to detect. There is a need for very sensitive detectors to detect such small signal. Hot-Electron Bolometer (HEB) satisfy one kind of sensitive detectors.

When the electrons can be described as thermally decoupled from the phonons, they can each have a different temperature. When the thermal coupling between the phonons and the electrons is weaker than the thermal coupling between the phonons and the substrate. This means that the electrons can heat up while the phonons stay cold, thus the term hot-electron. In this situation both, the electrons and the phonons, can be in thermal equilibrium each having its own temperature where the temperature T_e of the heated electrons is higher than the phonon temperature T_{ph}. Firstly, "hot-electron" term was used to describe non-equilibrium electrons in semiconductors (Al'ber, et al. 1976) Afterwards, this effect was observed in metals (Wellstood, et al. 1994) and superconducting systems (Perrin and Vanneste 1983).

The electrons and Cooper pairs are used as the absorber and the body of the bolometer in the superconducting HEB. And they are also used as the thermometer. The subsystem of phonon which is coupled to the thermal bath is used as the heat sink. When

radiation is absorbed in such a detector, the temperature increases and thus the resistance of the superconducting device changes (Perrin and Vanneste 1983).

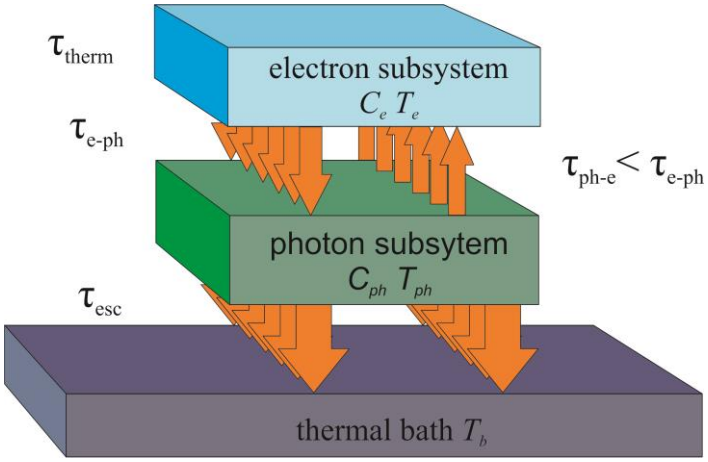

Figure 2.3. Schematic design of the energy transfer in a Hot-Electron Bolometer (Source: Semenov, et al. 2002)

Schematic design of thermal process of the electrons and phonons and their corresponding interaction times in HEB shown in Figure 2.3. $C_{e,ph}$ are the heat capacities and $T_{e,ph}$ are the temperatures of the electrons and phonons, respectively. According to (Semenov, et al. 2002) the time for the energy transfer from the phonon to electron subsystem τ_{ph-e} has to be much larger than the escape time τ_{esc} of phonons into the substrate for an effective decoupling of the electron subsystem from the phonon subsystem. The heat from the phonon subsystem is transported into the thermal bath. At the same time, the phonon-electron interaction time to prevent backflow of energy from the phonon to the electron subsystem has to be much larger than the electron-phonon interaction time τ_{e-ph}. The thermalization inside the electron and phonon subsystems is assumed to be instantaneous.

The detection of incoming radiation process in a HEB can be described as follows:

1. Photon breaks a Cooper pair or excites an electron when it is absorbed with an energy of $\hbar\nu$ in the HEB.
2. This case produces a highly excited electron which has almost the complete energy of the photon.

3. The electron loses its energy by emitting high energy phonons that in can turn, with sufficient energy, break other Cooper pairs or scatter with electrons.
4. This creates an avalanche effect of excited electrons that redistributes the energy of the absorbed photon inside the electron subsystem.
5. When the thermalization time τ_{therm} is much smaller than τ_{e-ph}, it can be assumed that the electrons have a uniform temperature T_e.
6. This thermal energy, on a timescale of τ_{e-ph}, can be transferred to the phonon subsystem which is at a temperature of T_{ph}.
7. When the stored heat capacity is transferred to the thermal bath with a temperature T_b, it is completely removed out of the system after a time τ_{esc}.
8. The time constant which for the energy backflow form the phonons to electrons is depending on the ratio of the respective heat capacities and can be taken from equilibrium conditions $\tau_{ph-e} = \tau_{e-ph} . \frac{C_p}{C_e}$.
9. The heat capacities of electrons and phonons (C_e, C_p) depend on the detector temperature.
10. While the phonon heat capacity below the Debye Temperature follows a power of three law $C_{ph} \propto T^{-3}$, the heat capacity of the electrons is inversely proportional to the temperature $C_e \propto T^{-1}$. (Kittel 1986)
11. The phonon heat capacity can become smaller than the electron heat capacity at too low temperatures and the hot-electron effect seizes to exist.

All time constant will be occur between the phonons, electrons and the substrate are material and temperature dependent. Thermalization inside electron subsystem preferred to have disordered material and temperatures which are as high as possible for the material to encourage scattering processes to achieve low electron-electron interaction time. The electron-electron interaction time can be written according to (Gousev, et al. 1994) as $\tau_{e-e} \propto \frac{1}{TR_{\square}} ln^{-1}(R_{\square})$. So, for a fast thermalization high operation temperatures and a large square resistance $R_{\square}$ of the film are required.

The strength of the interaction between phonons and electrons affects the electron-phonon interaction time. The temperature dependence of this interaction follows $\tau_{e-ph} \propto T^{-m}$(Bergmann 1984) where m is experimentally obtained parameter which varies between 1 and 3 for different materials. HEBs exhibit shorter relaxation times at higher

temperature supplies by this temperature dependency. Since an operation at higher temperatures is improving the speed of the HEB, materials with high T_c are better suited for use in HEB mixers.

2.1.3. Theoretical Model of the HEB

The response of a hot-electron bolometer to incoming radiation to describe the two-temperature model was developed theoretically (Perrin and Vanneste 1983). This model assumed that the thermalization of the electrons subsystem and the phonons subsystems happens instantaneous over the whole detector and a uniform temperature distribution can be assumed. The coupled heat balance equations of the respective subsystem defines the system. These equations are normally nonlinear but become linear in the case of a small signal excitation and close to T_C. The thermal balance equation for the electron subsystem can be written from using these assumptions (Semenov, et al. 2002)

$$C_e \frac{dT_e}{dt} = P_{inc} - \frac{C_e}{\tau_{e-ph}}\left(T_e - T_{ph}\right) \tag{2.10}$$

And for the phonon subsystem as

$$C_{ph} \frac{dT_{ph}}{dt} = \frac{C_{ph}}{\tau_{ph-e}}\left(T_e - T_{ph}\right) - \frac{C_{ph}}{\tau_{esc}}\left(T_{ph} - T_b\right) \tag{2.11}$$

where $C_{e,ph}$ are the heat capacities and $T_{e,ph}$ the temperatures of the electrons and the phonon respectively. The phonon-electron scattering time constant $\tau_{ph-e} = \frac{C_{ph}}{C_e}\tau_{e-ph}$ was taken from equilibrium conditions. When the energy of an electron has gone through the phonon subsystem and to the substrate, it is completely removed from the system. According to (Semenov, et al. 2002) the effective energy relaxation time of the electron can be described as

$$\tau_{e,av} = \tau_{e-ph} + (1 + \frac{C_e}{C_{ph}})\tau_{esc} \tag{2.12}$$

The dependence of the relaxation time of the HEB can be derived on the different parameters via equation (2.12).

2.2. Direct Detection of Radiation

When the direct detection used for the HEB, it is operated as a typical bolometer detector and reacts directly to the incoming radiation power. The detector does not different react between frequencies and polarizations. It acts as a power detector and only integrates over the incoming radiation power. Thus, the phase of the incoming radiation does not affect the detector.

To limit the spectrum of the detected radiation passive filters are used to filter out the desired spectrum. Frequency dependent information depends on the polarization of the radiation. This information is gathered from the radiation by application of external polarizers and spectrometers often in the form of tunable interferometers.

2.3. Antenna-Coupled Superconducting Bolometers

There are several possibilities to couple the radiation coming from the free space to the detector element. The most common method to transfer a free space wave into a current is an antenna which can work bi-directional. When it used as a transmitter, voltage is applied to feed point converting the electric field in units of Volt/meter. When used as a receiver, it picks up and electric field energy in units Volt/meter from electromagnetic waves in the medium, is converted to voltage difference on the tips of the antenna in units of Volt. Dipole antennas, bow tie antennas, horn antennas and spiral antennas are based on the type of log-periodic antenna.

Dipole antenna is composed of two equal arms which each have length of signal wavelength $X/4$. The V-shaped telescopic antenna is the most common type of antenna, used with television. The main advantages of bowtie antenna are broadband impedance and simple design. This antenna is defined only by the bow angle and frequency is independent if both sides extended to infinity. To produce an efficient bowtie antenna one

should have feed point which has limited bandwidth, resulting in a limited size (Gonzalez and Boreman 2005).

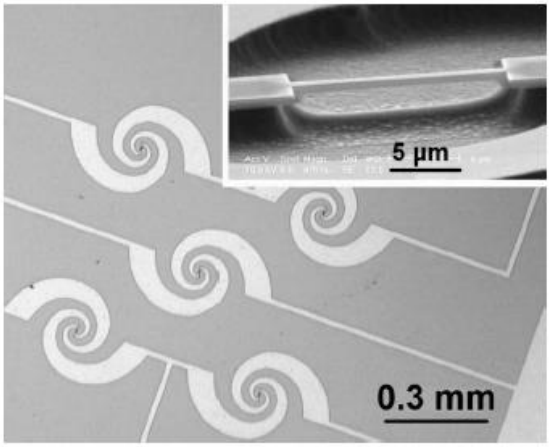

Figure 2.4. Spiral antenna designed with 5-membered low temperature superconductor bolometer (Source: Cibella, et al. 2009)

Spiral antennas are planar and may be circular or rectangular wound structure. While there are usually two-arm, multi-spoke design also can be seen. Spiral antennas are used in many areas such as mobile communication systems, early warning systems, underground imaging radars, navigation systems. They are nearly frequency independent, circular polarization, which can be designed in planar structure as well as conical, reflective or non-reflective elements are available.

Horn antenna is one of the most fundamental antennas. Due to the expansion of the walls of the outer surface of the antenna, the mismatch between the waveguide and free space is reduced (Thiele, et al. 1981). Carob antenna does not distribute the electromagnetic energy homogeneously in all directions. Here, part of the energy can propagate in a given direction, less energy spreads in other directions. Carob antennas are used in both ground and microwave communications in space.

2.3.1. Log-Periodic Antenna

Log-periodic antennas are independent of the frequency and this type of antenna was found by Duhamel and Isbell (DuHamel and Isbell 1957; Isbell 1960; Saijo, et al. 2001). A log-periodic antenna is formed logarithmic repeating element geometry in terms of the distance from the center point. Theoretically, both the outer elements and to the center point should continue indefinitely, even though in practice the antenna elements constituting the array from both sides, the required bandwidth cuts by considering.

Log-periodic antenna with fully open all the way unless stated are completely independent frequency. Planar log-periodic structure shown in Figure 2.5. Edges $\alpha/2$ specified angle is formed from a metal sheet.

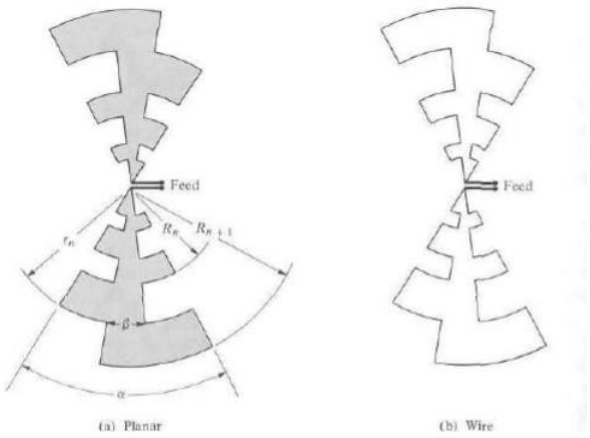

Figure 2.5. Planar and wire log-periodic antennas
(Source: Balanis 2012)

A typical log-periodic antenna structure is shown in Figure 2.5. Log-periodic antenna is composed of two co-planar structure. Models are unidirectional and towards the top of the cone formed by the two arms and linearly polarized. This and other log-periodic antenna structure completely independent frequency models although the width of certain designs and design variations are much lower.

A different log periodic antenna structure seems in Figure 2.6 (a). $\tau = 0.5$ was and the outer diameter of the antenna 1280 μm in this antenna structure. Scanning

frequency range from 50 to 1100 GHz (Saijo, et al. 2001). In addition, in Figure 2.6 (b), the central angle of the log periodic antenna structure is 45˚. This antenna has the minimum inner diameter 82 μm, maximum outer diameter 700 μm and τ ratio is 0.49. (Mendis, et al. 2004).

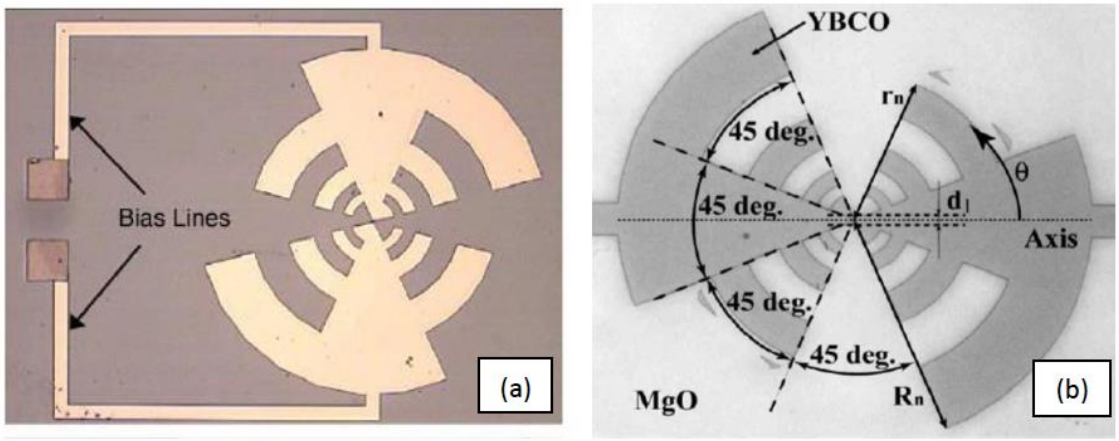

Figure 2.6. (a) Log-periodic antenna structure with circular gears and (b) Micro graphic of log-periodic antenna made from YBCO thin film (Sources: Saijo, et al. 2001; Mendis, et al. 2004, respectively)

Simpler and lighter, less expensive antennas have also been investigated. V-shaped non-planar geometries is used extensively by bending an arm compared to the other arm (Balanis 2012).

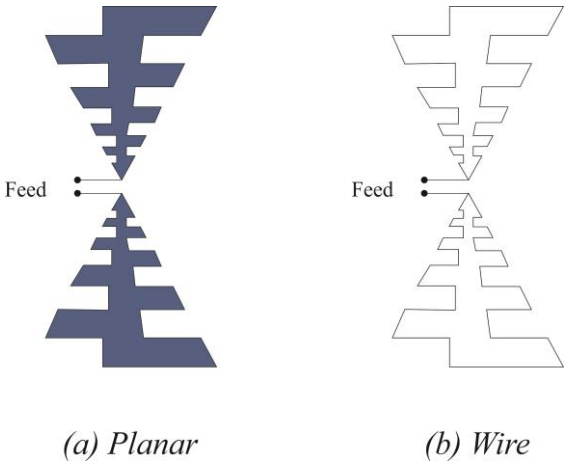

Figure 2.7. Planar log-periodic antenna and log-periodic antenna wire gear

If the wire or edges of plate is linear instead of curved, the geometry of Figure 2.5 is reduced to the trapezoidal thread log periodic structure of Figure 2.7. This simplification causes that more convenient geometry fabrication of the performance of work. Log-periodic antenna has many configuration including sequence. The formula of the geometric ratio of the log periodic antenna structure defined by following equation (Balanis 2012).

$$\chi = \frac{r_n}{R_{n+1}} \tag{2.13}$$

The width of the location of the antenna can be calculated with $\chi = \frac{R_n}{R_{n+1}}$.
Geometric rate of τ defines the operation cycle. So,

$$\tau = \frac{f_1}{f_2}, f_2 > f_1 \tag{2.14}$$

2.4. Noise in Bolometers

Hot electron bolometers used for the measurement of very weak energy signals. The noise generated by the receiver system and the background noise of the incoming radiation are limiting factor for signal measurement. When the signal of the incoming radiation is smaller than the noise signal, there is no measurement. Thus the reduction of the noise for the measurement of small signals is great importance.

2.4.1. Noise Equivalent Power

The noise equivalent power (NEP) is often used as a figure of merit to characterize the noise performance of detector systems when operated in direct detection mode. When using the NEP, it is possible to add and compare the different contributions of noise to the total. The NEP is defined as the radiation power P_{inc} incident on the detector which produces an output signal of the magnitude of the noise P_{noise} of the detector in a

bandwidth of one Hz. Adding the squares of the different NEP which arise from uncorrelated noise sources causes the total NEP in the detector. (Low and Hoffman 1963)

The noise in the detector has various sources (Richards 1994) such as photon noise from the background radiation, the Johnson noise and the phonon noise.

The total NEP and the Johnson noise of the bolometer can be written according to (Richards 1994)

$$(NEP)^2 = (NEP)^2_{Johnson} + (NEP)^2_{Phonon} + (NEP)^2_{Photon} \tag{2.15}$$

Random fluctuation of the electrons inside the bolometer due to the Johnson noise has a value as

$$(NEP)^2_{Johnson} = (4kTR)/|S|^2 \tag{2.16}$$

where k the Boltzmann constant, T the detector temperature, R the resistance of the bolometer and S the sensitivity of the bolometer. When increasing the sensitivity of the detector or reducing the resistance or the operation temperature, the noise contribution from the Johnson noise can be reduced. The niobium nitride hot electron bolometer needs to the fixed resistance and the operation temperature near T_c because of the matching to the antenna structure. The phonon noise term

$$(NEP)^2_{phonon} = 4kT^2G/\eta \tag{2.17}$$

where G is the coupling between detector thin film and substrate and η is the absorptivity of the bolometer, stems from the thermal fluctuations inside the bolometer which is caused by the phonons passing from the bolometer over the thermal conductance G to the substrate. When reducing the thermal coupling of the bolometer to the thermal bath which is also desired for an increased sensitivity, it can be suppressed.

The NEP contribution from the photon noise comes from the background radiation to the detector. To blocking the incoming radiation power in the unwanted frequency range, bolometric systems usually use filters with a transmittance $\tau(n)$. The total noise of the system increases due to incoming background radiation. The main reasons of the noise contributions are the characteristic of the incoming radiation source

and bolometer temperature. Thus detectors only limited by this noise contribution are called background limited detectors. All calculation for the NEP can be calculated in a thermal equilibrium. The phonon noise is the main contributor for real detectors. The thermal coupling of the film and the quality of the interfaces through which this thermal coupling happens has to be improved to reduce the phonon noise. This value corresponds to the NEP in a way that $T_N = NEP/k\sqrt{B}$ where B is the measurement bandwidth of the system. It is most commonly used when comparing different superconducting mixers.

2.4.2. Noise Temperature

The noise temperature T_{noise} is the most common used figure for compare the performance of different mixer devices in the THz range. To directly measure the noise temperature of a mixer setup the detector is pumped into its operation point by a local oscillator. Then the thermal radiation coming from a hot load (usually a black body radiator at room temperature) and a cold load (usually a black body radiator cooled down to 77 K using liquid nitrogen) expose to the mixer. This hot and cold load is measured to signal response of the detector. Using the Y-factor method the noise temperature of the system can be directly calculated. The detector is irradiated with two radiation sources with a well-known temperature and radiation power like the hot/cold load described above to calculate the Y-factor of a detector. The noise temperature can be calculated according to (Kerr 1999). The output power of the detector will then be

$$P_{out,hot/cold} = G\left(P_{in,\frac{hot}{cold}} + P_{noise}\right) \tag{2.18}$$

where G is the gain of the detector, $P_{in,hot/cold}$ is the radiation power of the hot/cold load and P_{noise} the noise of the detector in the bandwidth B of the system. The Y-factor is the ratio between the output power of the detector under hot and cold load $Y = \frac{P_{hot}}{P_{cold}}$. Combining this formula with equation (2.20), the Y-factor can be calculated to

$$Y = \frac{P_{in,hot}+P_{noise}}{P_{in,cold}+P_{noise}} \tag{2.19}$$

Solving this equation for P_{noise} the noise power can then in turn be calculated to

$$P_{noise} = \frac{P_{in,hot} - YP_{in,cold}}{Y-1} \tag{2.20}$$

The hot and cold load used to irradiate the detector is a blackbody radiator at liquid nitrogen temperatures $T_{cold} = 77\ K$ and one at room temperature $T_{cold} \approx 300\ K$. Then the noise temperature can be easily calculated to using the Rayleigh-Jeans law $P = kT$ where k is the Boltzmann constant.

$$T_{noise} = \frac{T_{hot} - YT_{cold}}{Y-1} \tag{2.21}$$

When devices characterized at very high temperatures, the Rayleigh-Jeans law is still valid. Kerr suggested (Kerr 1999) that operation temperatures of the devices are close to absolute zero when incoming high radiation frequencies. To account for this discrepancy the physical temperatures in formula (2.21) have to be corrected because of devices close to the quantum noise limit. So, the physical temperatures $T_{hot,cold}$ have to be replaced by the Callen and Welton definition (Callen and Welton 1951)

$$T_{C\&W} = T\left(\frac{\frac{hf}{kT}}{\exp\left[\frac{hf}{kT}\right]-1}\right) + \frac{hf}{2k} \tag{2.22}$$

in order to derive the noise temperature which accounts for zero fluctuation noise $\frac{hf}{2k}$.

CHAPTER 3

EXPERIMENTAL

3.1. Bi2212 Single Crystal

Structural characteristics of the high-temperature superconductors have a significant effect on superconductivity. All ceramic superconductors consist of the similar layers which are closely related to classic perovskite ABO_3 structure. One of these layered is Bi-based high temperature superconductors. Superconductors in this structure is given by the general formula $Bi_2Sr_2Ca_{n-1}Cu_nO_{2n+4+\delta}$ wherein n refers to number of perovskite unit or units within the cell number of the copper oxide layer. Bi-based high temperature superconductors have 3 different phase and critical temperature values. For n=1 $Bi_2Sr_2CuO_{6+\delta}$ (Bi2201) and $T_c \leq 20$ K (Yurgens 2000), for n=2 $Bi_2Sr_2CaCu_2O_{8+\delta}$ (Bi2212) and $T_c \approx 95$ K and for n=3 $Bi_2Sr_2Ca_2Cu_3O_{10+\delta}$ (Bi2223) and T_c=110 K. These natural layered structure shows much better characteristics than achieved artificially (Sischka 2002). Due to the structure of high temperature superconductors shows anisotropic properties for critical areas, resistivity, and etc. parameters. Bi2212 phase has greater than 100 of the Ginzburg-Landau parameter κ, and this Bi2212 phase indicates strongly type 2 superconductors (Michishita, et al. 1996). Bi2212 consists of Bi-O and S-O insulating layers which are lined in layers of CuO_2. The nature of Bi2212 is dependent on the different arrangements of Cu-O, Bi-O and S-O layers. To explain this structure is multi-layered and proximity named two models have been proposed (Revcolevschi and Jegoudez 1997).

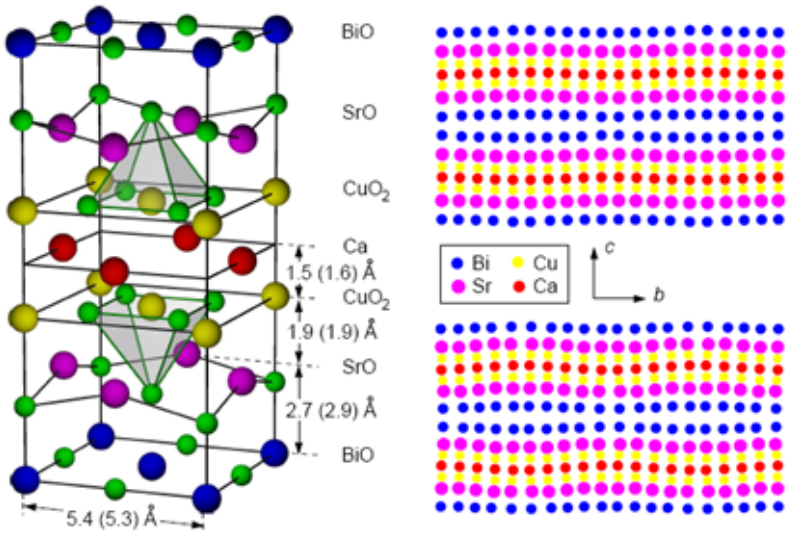

Figure 3.1. Crystal structure of Bi2212 and crystal structure from x-ray diffraction (Source: Disorder in Unconventional Superconductors, 2003)

According to multi-layered Bi2212 model, structure composes of the overlaid arrayed 3Å C-O double layers, and this layer is separated by Sr-O and Bi-O layers which have the non-superconducting and 12Å thickness. In proximity model, not only CuO layer, Bi-O and CuO layers contribution of the superconductivity together. Some experiments showed that Bi-O layer may act like insulating property instead of semi-metal or superconductor. By proximity effects, between Cu-O and Bi-O layers have a strong coupling and between Bi-O layers are the weak Josephson coupling. Structural anisotropy and the presence of Cu-O layers greatly affects the physical properties of the BSCCO family. Bi2212 anisotropic single crystal can be separated along the a-b plane without damaging the main structure. In the following sections of this procedure are given information about how it is done.

3.1.1. Doping Dependence of Bi2212 Single Crystal

It is well known that the chemical composition and carrier concentrations are related to the physical properties of high temperature superconductor cuprates. The carrier concentration of the superconductor can be varied by doping process in like semiconductor materials. Doping process typically refers to introduction of impurities or charge carriers that can be holes or electrons.

The parent states of each family of cuprates are antiferromagnetic Mott insulators with one hole per planar copper (Taillefer, et al. 1997). The conductivity vanishes as temperature tends to zero in a Mott insulator which is transformed into metals and then superconductors by doping with charge carriers.

When carrier concentration is increasing, they all have an antiferromagnetic phase near zero doping. Then the superconducting transition temperature rises from zero to maximum and finally drops to zero again. All cuprates have the same phase diagram schematically shown in Figure 3.2.

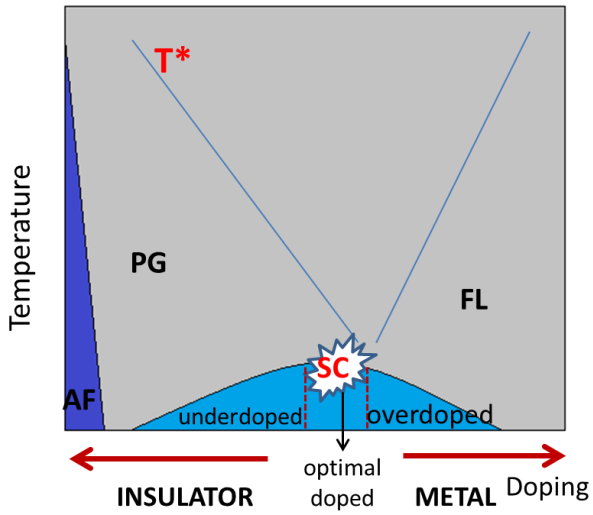

Figure 3.2. The phase diagram with doping in high-T_c cuprates superconductors

The two regions of the phase diagram, antiferromagnetic insulating state (AF)-below 320 K with hole doping $\rho \leq 0.02$ and the superconducting state (SC)-below 100 K and ρ is between 0.06 and 0.26 are well-established. The superconducting region in the phase diagram can be classified into three different regions; the insulating phase is usually called to underdoped region where T_c is an increasing function of carrier concentration. When they are optimally doped where T_c reaches its maximum and they are overdoped for larger carrier concentration. Some superconductor properties such as critical current density, transition temperature, the structural and flux pinning properties can be altered by doping level to obtain optimum superconducting material. Carrier concentrations of superconducting cuprates can be varied by adding excess oxygen atoms or by reducing oxygen atoms without changing crystalline structure. Although hole-doping is the rule in

high-T_c superconductors there are some cases where the mobile charges are electrons. The phase diagram of the electron-doped HTS is qualitatively similar to the phase diagram of the hole-doped HTS.

The doping dependence of high temperature superconductor Bi2212 single crystal has an important effect on superconducting properties such as energy gap and the superconducting energy gap of optimally doped and overdoped Bi2212 crystal is found to be smaller than the underdoped samples. Furthermore, it is known from studies of Miyakawa et al., the energy gap value is decreasing when the hole doping is increasing. (Miyakawa, et al. 1998)

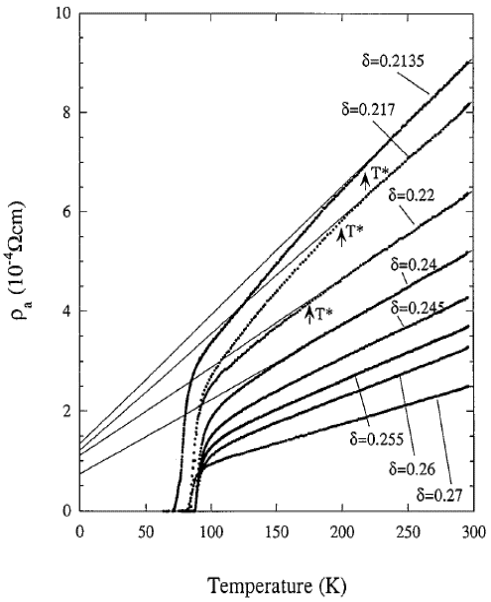

Figure 3.3. In-plane resistivity (ρ_a) of a $Bi_2Sr_2CaCu_2O_{8+\delta}$ single crystal versus temperature for various oxygen contents (ρ) (Source: Watanabe, et al. 1997)

The optimally doped samples of Bi2212 have approximately an onset critical temperature of 90 K. Figure 3.3 shows the temperature dependence of in-plane resistivity ρ_a for $Bi_2Sr_2CaCu_2O_{8+\delta}$ with different oxygen contents. The sample with δ= 0.27 shows T_c= 84 K. While δ is decreasing, T_c is increasing and it comes to overdoped state with highest critical temperature value (optimally doped) T_c= 89-90 K with δ= 0.24-0.25. With δ is more reducing ($\leq$ 0.22), doping gives underdoped states with T_c= 75-80 K.

3.1.2. Growth of Bi2212 Single Crystals

There are many production process of the produce Bi2212 single crystal superconductor such as sintering and melting the superconductor compounds. Even though the fabrication of HTSs by sintering process is easy, this method is only preferred for the bulk HTSs and these superconducting materials have porous structure and random arrangement of superconducting grains. Therefore it is difficult to obtain a smooth structure including the uniform orientation of the superconducting crystal completely on the bulk HTSs (Michishita, et al. 1996). In order to produce the layered HTSs with the high quality the researchers use the melting processes such as KCl flux method (Katsui 1988), vertical Bridgman method (Ono, et al. 1988) self-flux method (Shishido, et al. 1989, Tanaka, et al. 2001), melt-textured growth method (Jin, et al. 1988), the laser-heated pedestal growth method (Feigelson, et al. 1988) and travelling solvent floating zone method (TSFZ) (Takekawa, et al. 1988). In our work, we use Bi2212 single crystal which is growth TFSZ method. We can see the illustration of experimental setup in Figure 3.4.

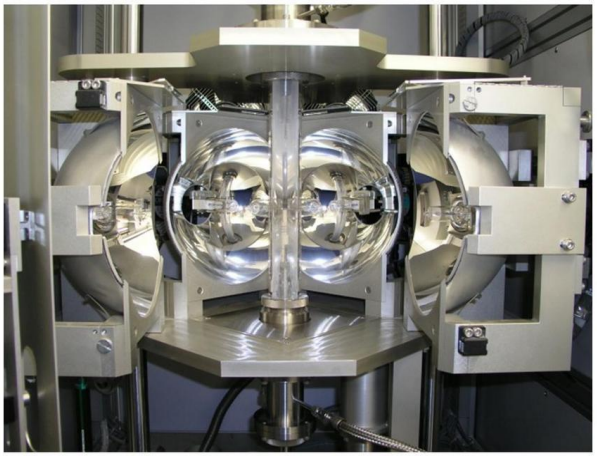

Figure 3.4. A photograph of an optical floating zone furnace

This method which is one of the melt processes is used to obtain high quality single crystal of HTS. During the process the layered superconducting structures with high purity are fabricated without contamination, because it is a crucible-free technique and compounds are heated by IR radiation in optical system. Growth of better crystals with large size dimensions and uniform aligned structure than the bulk structure of this materials is the most important property of the fabricated materials by the TSFZ.

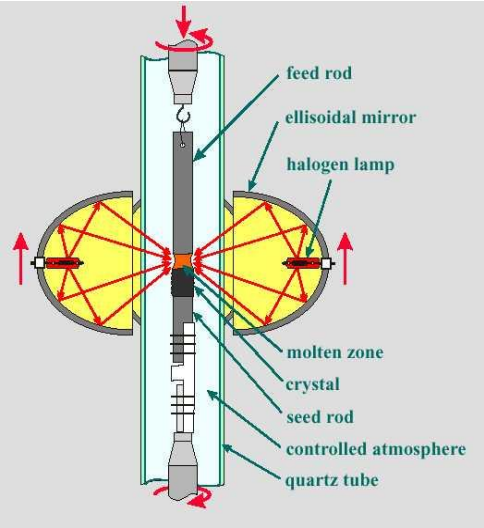

Figure 3.5. Principle of traveling solvent floating zone method
(Source: Crystal Growth, 2001)

In this technique, two halogen lamps located at one of the two focal points of the each ellipsoid chamber emit radiations that are focused by ellipsoidal reflectors to the other common focal point of each ellipsoid in which is molten zone. Before the floating zone process, by using calcination and sintering processes, the superconducting bulk material formed as a rod is prepared. To use as the feed and seed crystal rods in ellipsoidal furnace, the superconducting rod is divided into two pieces. Then they are coaxially mounted inside the quartz tube and their junction is in the center of the common focus point of each ellipsoid. The junction of two rods which is in molten zone which is heated by halogen lamps so they begin to melt. By obtaining refractory oxide single crystals, the rods are moved downwards at fixed speed. Thus superconducting crystal is solidified with unidirectional growth. During the growth, feed rod and seed crystal rods are rotated to obtain the homogeneous aligned crystal structure. The superconducting layered single crystal rod with Bi2212 phase whose growth direction is parallel to [110] a-b plane is obtained at the end of the TSFZ. The crystals have not only a layered structure with a-b alignment along to growth direction but also c-axis alignment in the transverse section. The crystal growth in the quartz tube is performed in O_2 gas flow to supply oxygen to crystal. The pressure of O_2 is used as one of the growth parameters since it is affected the growth temperature and stabilization of the molten zone (Michishita, et al. 1996).

3.2. Bolometer Fabrication

In this study we used many techniques such as chemical process, annealing, thermal evaporation, clean room process, e-beam lithography etc. Here, I will introduce briefly them.

3.2.1. Preparing of Thin Bi2212 Single Crystal by Exfoliation

$Bi_2Sr_2CaCu_2O_{8+\delta}$ crystalline passes through many intermediate steps before the application form (Wang, et al. 2012). Uneven in the upper layer structure crystalline layers are removed carefully with a sharp-tipped blades. In the following process, crystalline is transferred and thinned steps with using different methods. One of them is transferred method.

Transferred Method: Scotch tape adhered to separated crystal layers carefully. Until the desired degree of crystal surface and thinness are made separating layer by layer with tape (Kakeya, et al. 2008). Method is shown in Figure 3.6.

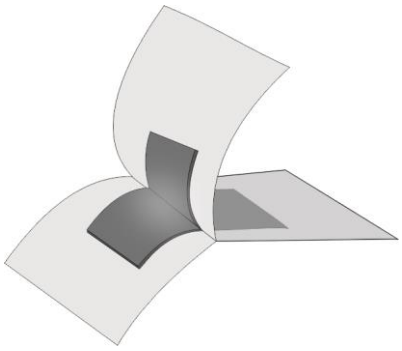

Figure 3.6. Mechanical exfoliation method

The crystal layer is more smoothly separated. When the crystal came to the desired state, it is pasted to sapphire with scotch tape. During the gluing step important to pay attention to the Bi2212 single crystal layer bonding without causing any stress. Bonded to the sapphire sample is chemically treated immediately.

Chemical Method: Our goal is to transfer to our film on sapphire without any adhesive. Therefore, it is important to select the right chemical for get rid of all tape and its remains. We made research on the structure of the tape and has been tried many alternatives before finding the right chemicals. Some of these limonene, acetone, tetrahydrofuran, chloroform, dimethylsulfoxide. Chloroform and tetrahydrofuran are selected from these chemicals. Solvent time and without leaving a residue of solving have been effective when selection is made. After selecting the correct chemicals, these chemicals are filled to containers about 10 to 15 mL. Then the sample slowly released into the containers with tweezers and band is separated from the film with the help of an ultrasonic. At the end of process residues are made examination under a microscope. If the residue remains on the sample, treatment is continued for a certain period. Without any residues and different sizes surface is obtained. (Figure 3.7)

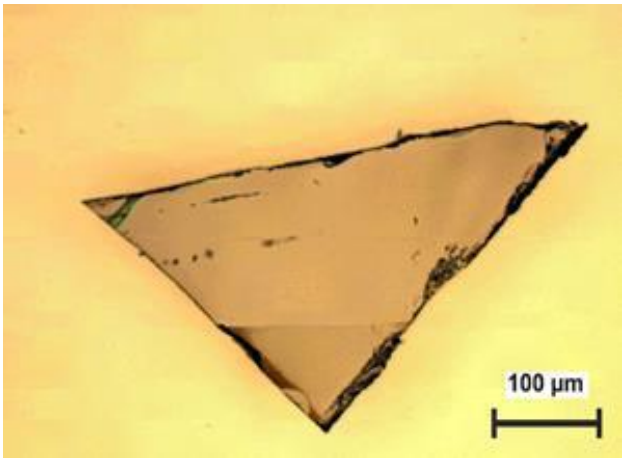

Figure 3.7. Transferred Bi2212 single crystal on the sapphire

The film surface is quite smooth, and used for the transfer process from tape no remains are left as can be seen in the figures. The same situation can be observed clearly in SEM image in Chapter 4.1.2.

Different sizes and different thicknesses of films can be obtained with this method. In Figure 3.8, one of the films obtained on Si substrate.

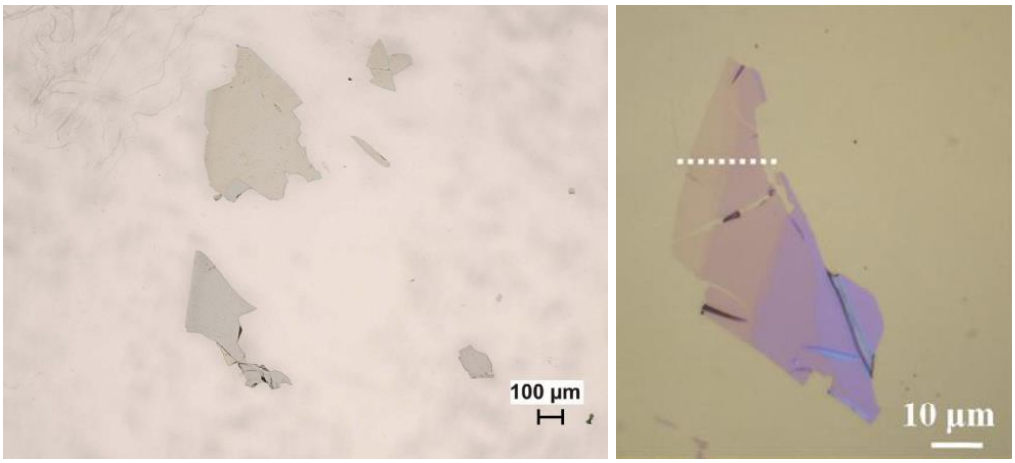

Figure 3.8. Left picture is our film on sapphire substrate, right picture is obtained in a different work with different technique (Source: Kakeya, et al. 2008)

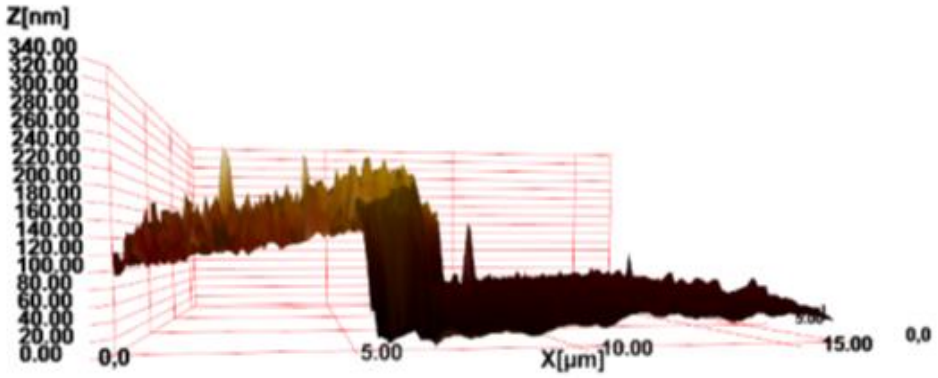

Figure 3.9. AFM image of the sample with a thickness about 180 nm

It possible to achieve smooth surfaces in this way. The thickness of the films obtained are between 70 nm and 180 nm. In Figure 3.9 shows measurement results that obtained using the dynamic mode AFM. And also we can calculate the thickness from the number of layers via I-V measurement. Each graph represents the one layer and each layer has 1.5 nm thickness. Then when 1.5 nm times number of layers give us the total thickness of the crystal.

3.2.2. Annealing of Bi2212 Single Crystal

Many scientists have made extensive efforts to understand the structure of high temperature superconductor materials after the discovery of Bi-based superconductors by Maeda et al in 1988 (Maeda, et al. 1988). It is well recognized that Cu-O planes in the high temperature superconductors have an important role in determining of carrier concentration which provides important knowledge about physical properties of high temperature superconductors. The oxygen site occupancy should be altered by annealing process with controlled oxygen partial pressure to control the carrier concentration of cuprates. Here, oxygen non-stoichiometry is very crucial parameter to control critical temperature of Bi2212 single crystal. It is shown that the critical temperature of Bi2212 crystal can be changed significantly by controlled heat treatment in different atmospheres (Genoud et al. 1995). When the oxygen concentration is lower or higher than the optimal one, the crystal said to be underpoded or overdoped, respectively. Three different atmospheres such as argon, vacuum, or oxygen can be used to control oxygen level of Bi2212 crystal.

Our transferred Bi2212 single crystals were annealed with various parameters in order to make optimum. Therefore, crystal annealing process was performed in a tube furnace with a quartz tube. The air and oxygen media were used to annealing parameters (Yamada, et al. 2007). First annealing parameters are an oxygen atmosphere at a pressure of 1 atm for 30 minutes at 400^{o}C and 2 sccm oxygen delivery by MKS (Figure 3.10). The other annealing parameters were performed at 400^{o}C for 1 hour in air medium as seen in Figure 3.11.

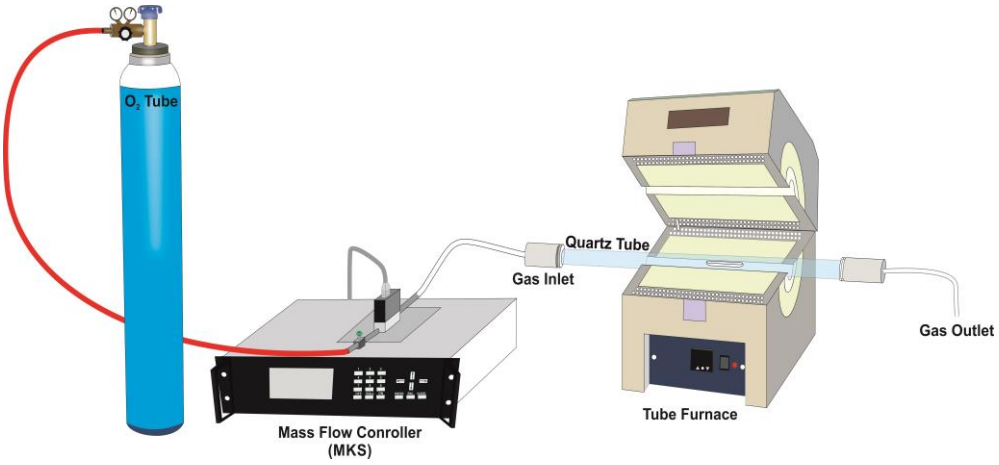

Figure 3.10. Our annealing system with oxygen atmosphere

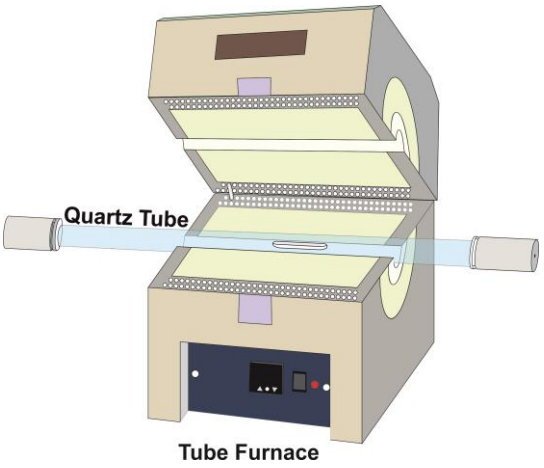

Figure 3.11. Our annealing system with air atmosphere

However, we have determined that oxygen annealing of as-grown Bi2212 samples is not good enough because we change oxygen concentration from as grown to underdoped or overdoped. To make annealing process easy we continue with air anneal. R-T results will show in Chapter 4.2.1.

3.2.3. Thermal Evaporation

At the same time we deposited gold with aluminium mask for R-T measurement and without any mask for antenna process. After sample was transferred and annealed,

the sample is immediately placed in vacuum chamber to evaporate 150 nm gold layer onto it. Gold layer protects the fresh and smooth layer of Bi2212 from chemicals such as photoresist, developer and water during the lithography. In addition, it is very useful to get electrical contacts for characterization. Schematic representation of the vacuum thermal evaporation system that we have used to deposition of Au layer on cleaved Bi-2212 single crystals can be seen in the Figure 3.12. Evaporation technique is based on two basic processes which are evaporation of material in a filament boat with 105-110 A and then condensation on the cooler substrate. Generally low pressure about 10^{-6} Torr is preferred to avoid reaction between the vapor and atmosphere during the evaporation because of the mean free path of vapor atoms and the vacuum chamber dimensions are approximately same, so, it results in traveling of particles in straight lines from the source to substrate. The deposited film thickness and the rate of deposition are controlled by a thickness monitor during the deposition.

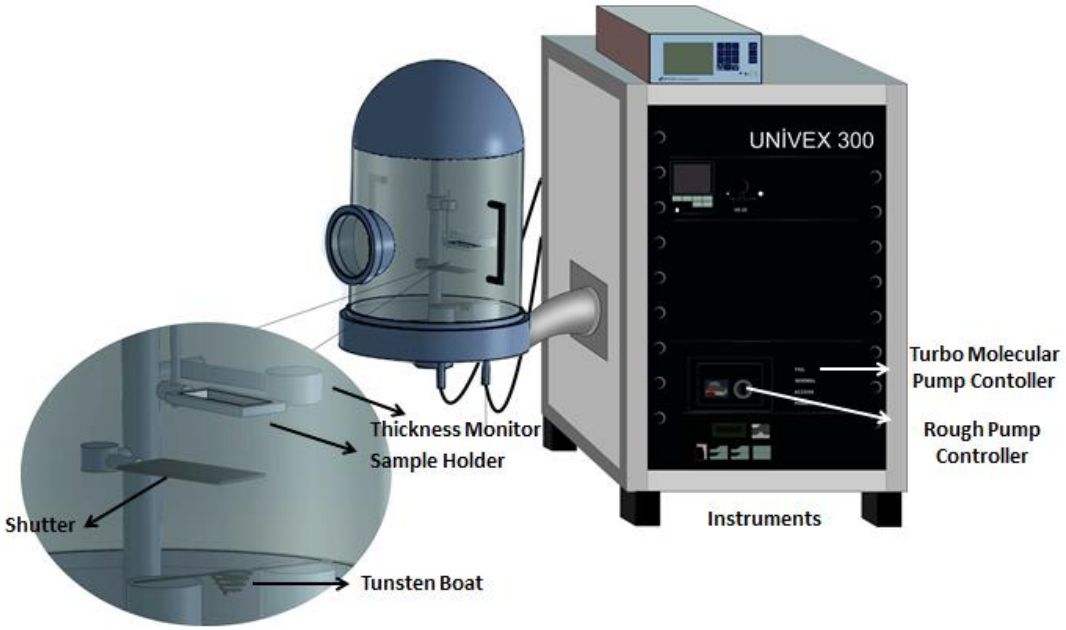

Figure 3.12. Schematic representation of our thermal evaporation system

Vacuum thermal evaporation technique has many advantages; the average energy of vapor atoms, which are reaching the cooler substrate, are generally very low, in the order of kT, i.e. tenths of eV. Very high purity of thin films is provided by high vacuum environment. Furthermore, the deposition rate is high and the technique has fewer tendencies for unintentional substrate heating.

3.2.4. E-Beam Lithography Process

Electron beam lithography provides scientist to design, place elements at the smallest possible scale and very useful technique to produce extremely fine patterns (~50 nm). This technique enhanced from the scanning electron microscope which has scanning a beam of electrons across a surface covered with a resist film, which is sensitive to those electrons. E-beam lithography provides very high resolution for patterning process such as at the nanometre scale and it does not require a photo mask unlike classical photolithography process. However, e-beam lithography technique has some limitations with such precision. Firstly, patterns can only be obtain in a long period of time and it is a disadvantage for commercial acceptance. Besides, since electrons are charged particles, e-beam lithography requires high vacuum conditions so it further complicates the required equipment and processes.

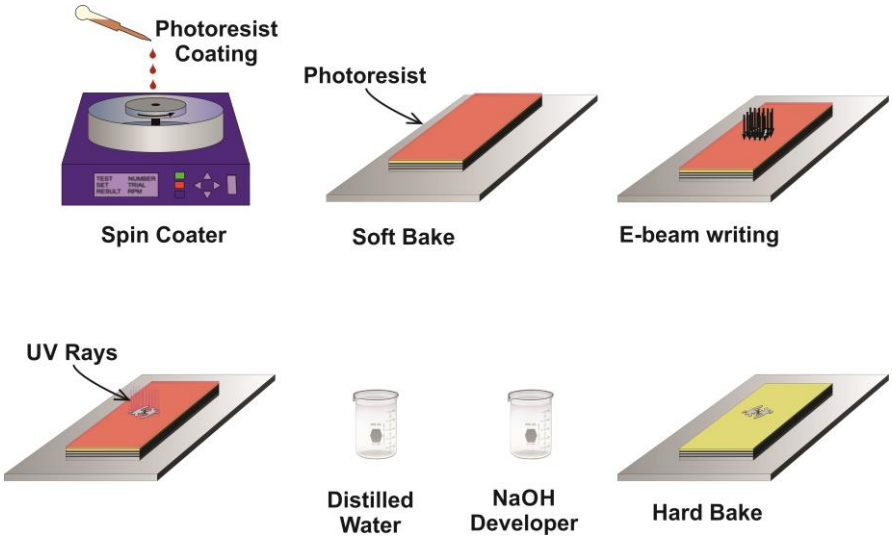

Figure 3.13. Schematic representation of e-beam lithography processes

Then, about 2 μm AZ5214 type photoresist layer is formed on the sapphire by using the spinner at 3000 rpm for 50 seconds in the clean room. Sapphires are baked for 30 minutes at 90^{o}C by using the technique of so-called soft-baking. After here, for the patterning of log-periodic antenna was formed using electron beam lithography. Figure

3.14 represents the e-beam lithography system that we used to fabricate the log-periodic antenna structure.

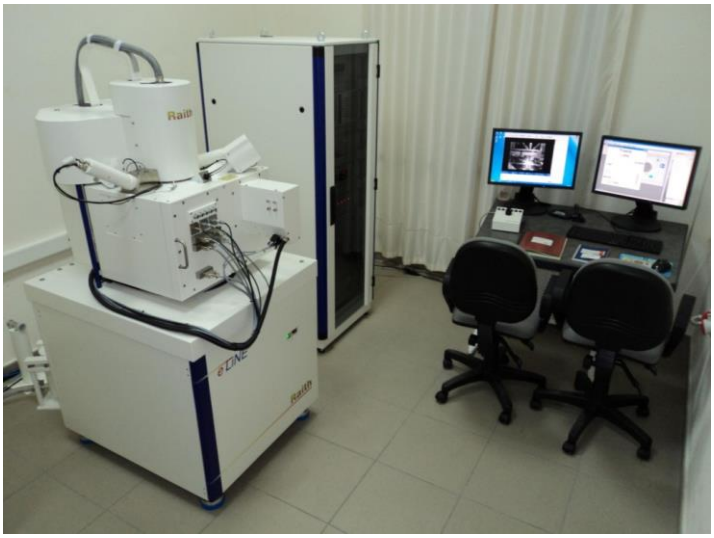

Figure 3.14. Picture of our electron beam lithography system

Afterwards, sample is exposed to UV lights for 7 seconds and then immediately developed in 2 M NaOH solution for 5 seconds. Before starting etching process, firstly sample is hard baked in an oven at 120^{o}C for 30 minutes. The schematic diagram of the e-beam steps can be seen in the Figure 3.13. Now, sample is ready for etching.

3.2.5. Ion Beam Etching

Chemical and dry etching processes are the most commonly used methods in micron-sized fabrication of materials in many etching techniques. Undercutting of films, limiting lifetime due to contamination, roughness and pitting and chemical reactions with other materials and surface are disadvantages of chemical etching processes. Because of all this reason, this technique is not suitable and useful for patterning of antenna structures. On the contrary that, ion beam etching technique is a stress free physical process whereby an ion source is used to produce broad ion beam, which are directed to the substrate for etching purposes. Argon atoms are ionized in a chamber by electron bombardment. Here electrons are generated by a cathode filament and then collected by the anode. Generally a magnetic field is used to direct the electrons to the right place and

to increase the probability of etching. A turbo molecular pump with a rough pump is used to reach the pressure value of 10^{-6} Torr because of low pressure is necessary to decrease the contamination of substrate during etching process.

In our experimental setup, samples are placed inside the etching chamber with an angle of 67.5º. Figure 3.15 illustrates our ion beam system in our laboratory. Firstly etching chamber is pumped using a turbo molecular pump with back pump until the pressure value of 10^{-6} Torr before starting the etching. Because low-pressure values are required to increase the mean free path of ion beam accelerating from the ion source. When desired pressure values are reached, firstly 30 sccm argon gas, which is controlling mass flow controller, is introduced to the system. Afterwards, a DC source is applied to obtain plasma inside the etching chamber and a rotational feed through mechanism is used to prevent the differences in lateral angles of mesas. During etching process, accelerated argon ions and crystal atoms collide each other and produce heating. Therefore, we have used a cooling system to cool the sample holder to prevent the heating occurrence throughout the etching experiments. Since the protected area is not etched, the sample is placed in acetone to clean up remained photoresist.

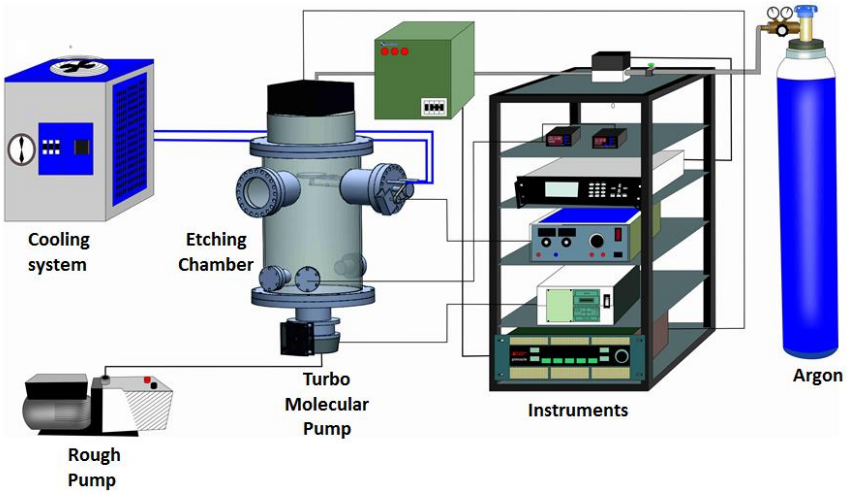

Figure 3.15. Schematic picture of our ion beam etching system

3.3. Characterization Methods

In this section, characterizations methods will be explained briefly.

3.3.1. R-T Measurements

A-B axis resistance versus temperature (R-T), and current-voltage behavior (I-V) were measured in a He flow cryostat system for characterization of fabricated antenna structures. In our continuous flow cryostat system has a closed cycle cooler which is used to decrease the temperature of fabricated antenna from room temperature to 20 K. He gas is compressed to 16.5 bar using a water cooled compressor to expand it in the cold head for cooling the sample. The compressed He gas is transferred by a flexible line to the cryostat. The sample temperature on cold finger is controlled by heater and temperature sensor that are interfaced by a temperature controller. Low-pressure values before beginning the measurement is used to create a thermal isolation and prevent the cooling system form ambient thermal effects in this system. The closed cycle cooling system has many advantages such as that it is very economical system, which includes closed cycle cooling without loss of He gas.

Schematic representation of the measurement system can be seen in Figure 3.16.

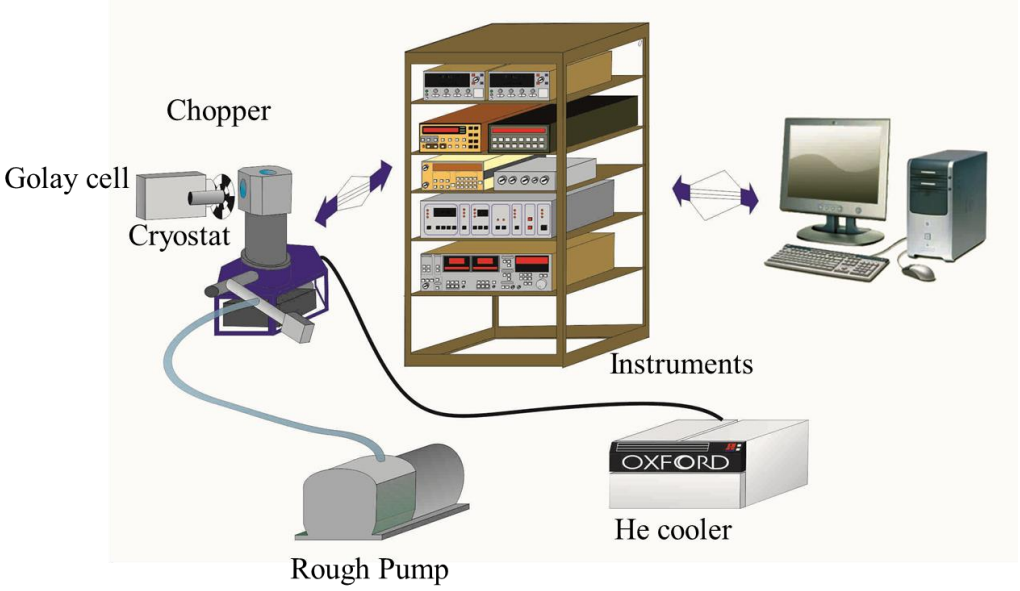

Figure 3.16. The schematic of our He flow cryostat system

We have done resistance versus temperature and current versus voltage measurements to characterize the samples by using the system mentioned above and shown below. The He flow cryostat system is controlled by a program written in Lab-view which is also used to analyze and storage of obtained data (Figure 3.17).

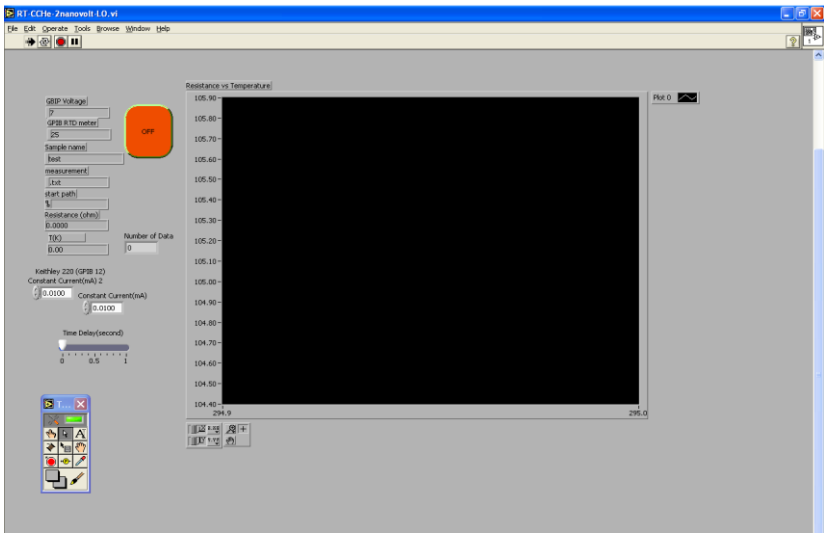

Figure 3.17. The screen image of Labview program used during the measurement

When the temperature is decreased using a closed cycle cooling system, the variations on the Bi2212 single crystal resistance is measured. The R-T measurement system consists of a voltmeter, current source and temperature controller. The applied current value is kept constant during the R-T measurement. To obtain more precise results, current is applied from both positive and negative side rapidly using a current source. After that the average value of the resistance is found by Labview program.

3.4. Cryostat Design for THz Detection

We have done the cryostat design and the production works. Cryostat has two main parts; main chamber and inside the main chamber. Main chamber consists of 250 mm height, 200 mm diameter, one electrical connection port, one THz wave input window and one vacuum station. Inner chamber has 153 mm diameter, 150 mm height and 23 hole for chips. Firstly, when we combined all parts of cryostat, we performed vacuum test and cryostat passed successfully. After that, the liquid nitrogen placed into cryostat and vacuum has been observed that how it is change. Cryostat liquid nitrogen reservoir contains about 3 litres. The vacuum is 1.0×10^{-4} Torr before being placed liquid nitrogen and the vacuum decreases to 5.8×10^{-5} Torr with cooling process. A schematic design of our cryostat can be seen in Figure 3.18.

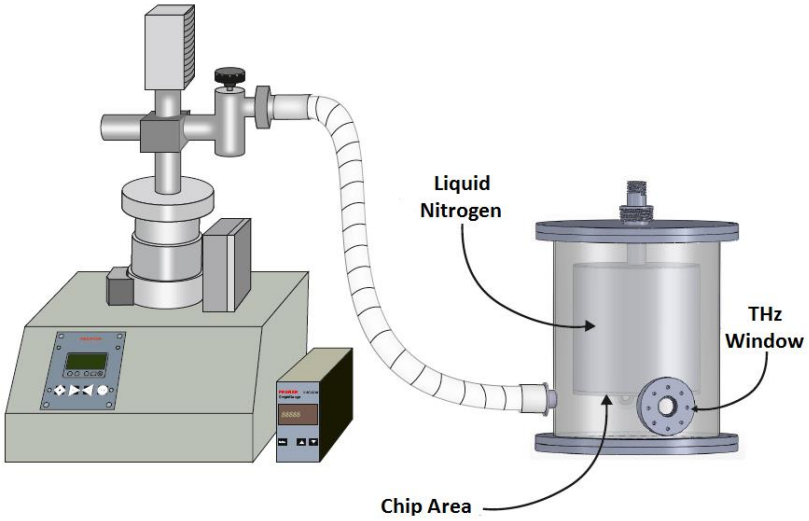

Figure 3.18. Schematic image of our designed cryostat

The wave collector was placed into the cryostat to focus incoming THz wave on the chip. Lake Shore Cernox thermal sensor purchased and placed with resistance values at room temperature 83.7 Ω and under a Liquid nitrogen atmosphere 300 Ω. R-T measurement of Lake Shore Cernox thermal sensor as in the Figure 3.19.

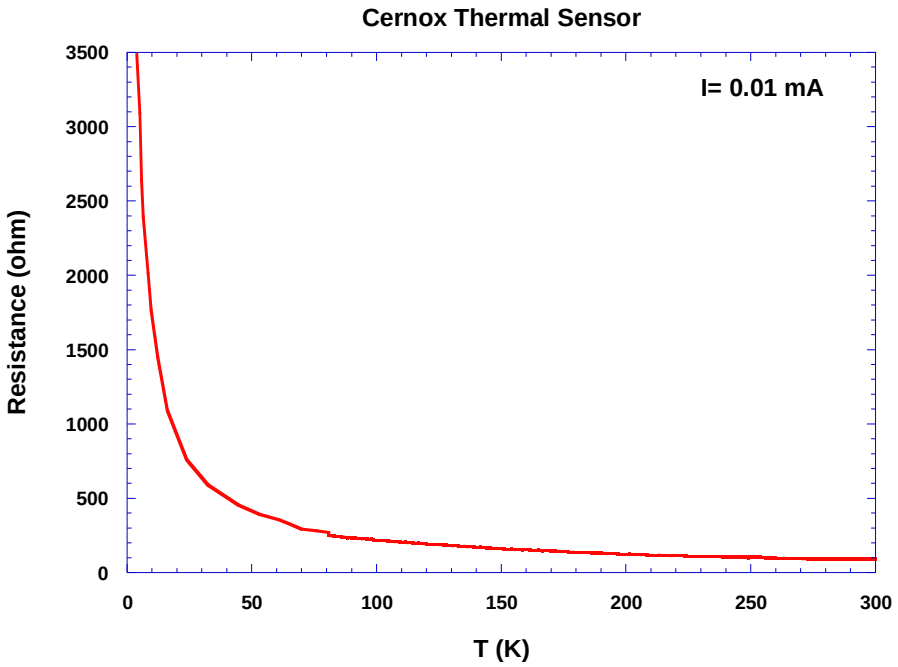

Figure 3.19. R-T measurement of thermal sensor

Then, a heater with the value of the initial resistance of 120 Ω was placed, as long as the system works, we want set the temperature in the cryostat. Electrical connections of the Cernox thermal sensor and heater were made and connected to Lake Shore 335 Temperature Controller. During this link 10 pin connectors and 0.15 mm thick copper wire were used. 5 copper wires with 10 ends are stranded and wrapped around the liquid nitrogen chamber. 4 of them goes to Cernox thermal sensor, 2 of them connected to sample and 4 connected to Heater from 10 copper wire ends which has been obtained. Inside images of the cryostat like in Figure 3.20.

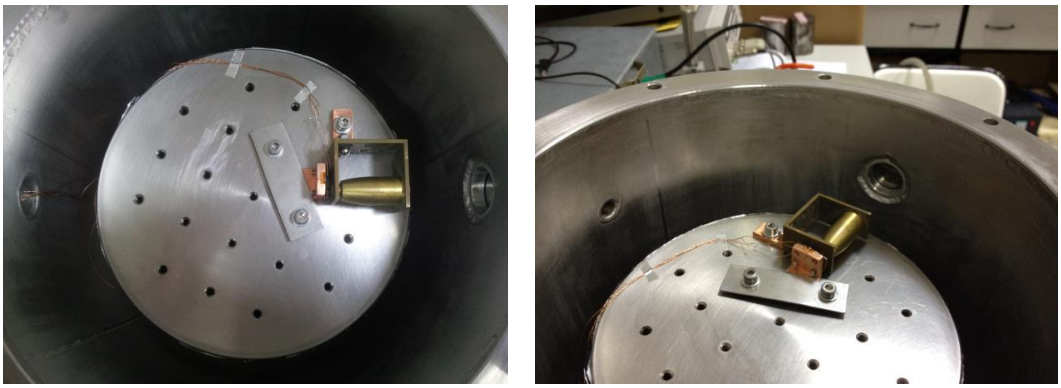

Figure 3.20. Wave collector, sample holder, Cernox thermal sensor and heater

Temperature Controller, which made the connection, connected to the computer with GPIB cable and computer programs written in Labview (Figure 3.21) allows us to adjust and control the temperature of the cryostat.

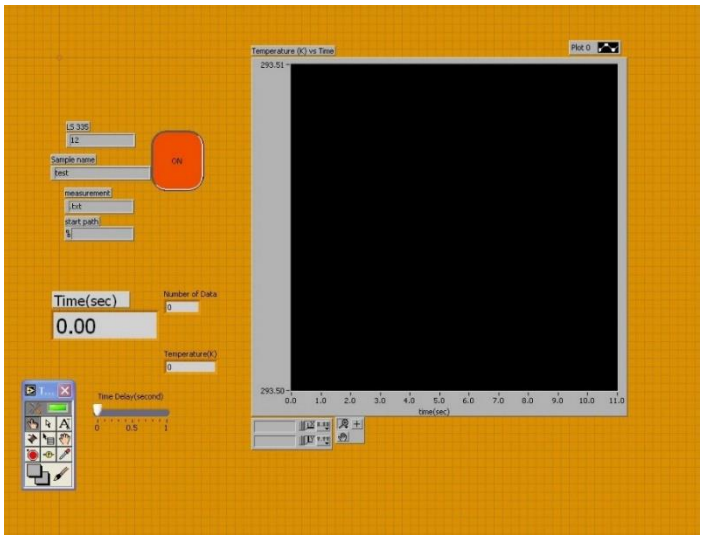

Figure 3.21. Lab-view screen image for temperature controller of cryostat

Cryostat being tested while in this time placed in the vacuum environment of how long the liquid nitrogen has been found to be contained within cryostat. This determination is made by determining the temperature inside cryostat from the temperature controller at vacuum environment with liquid nitrogen. Nitrogen has been found to be maintained for about 22 hours in the system. Then accounts for the further improvement of this time, as shown in Figure 3.22, the liquid nitrogen reservoir was coated with 15 μm thickness metallized film for 4 times. Application metallized film was reduced evaporation rate from 0.15 liter/hour to 0.085 liter/hour at the system is not running.

Figure 3.22. Liquid nitrogen reservoir coated with metallized film

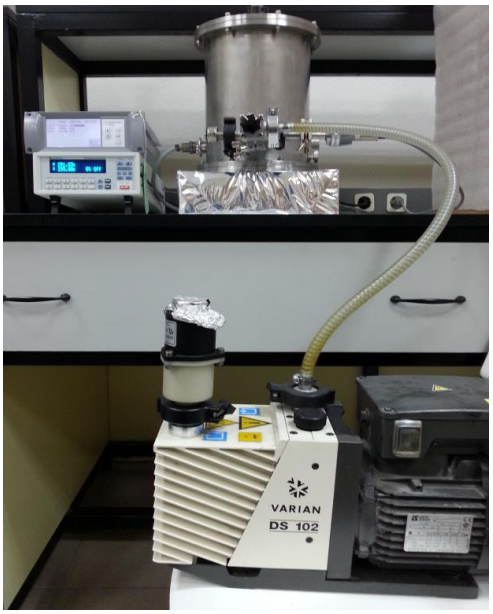

Figure 3.23. Temperature controller and vacuum gauge connection on the cryostat

The resulting ratio of liquid nitrogen is kept for 30 hours at a temperature of 77 K in the chamber. The test process the maintaining liquid nitrogen in cryostat is shown in graph form in Figure 3.24. Agilent Technologies Vacuum Controller connected to cryostat which have been allowed to read varying vacuum values (Figure 3.25).

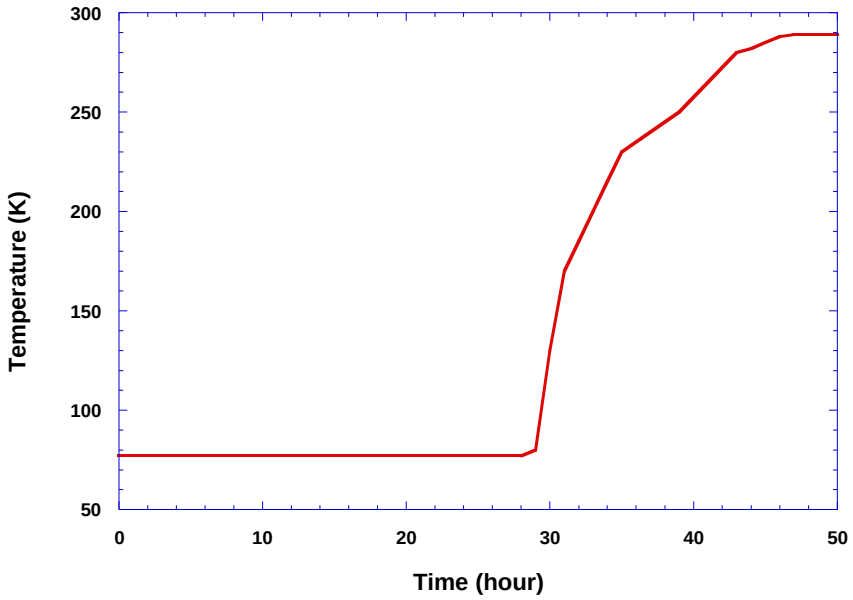

Figure 3.24. Liquid nitrogen storage period in the cryostat

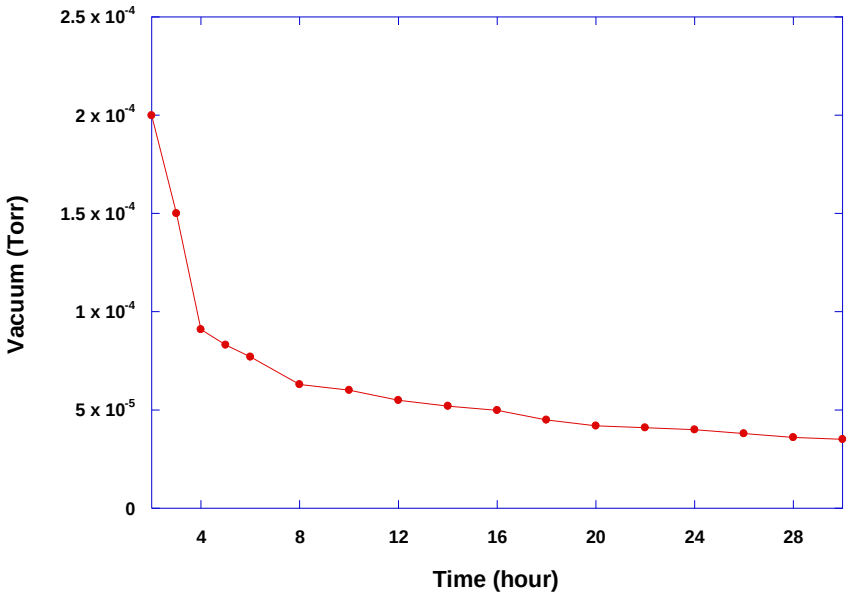

Figure 3.25. Vacuum values change with the addition of liquid nitrogen

CHAPTER 4

RESULTS AND DISCUSSIONS

4.1. Structural Characterization

In this section of the thesis, I will discuss the structural characterization of the fabricated thin Bi2212 and antenna structures. Surface profilometer and atomic force microscope were used to obtain the exact thickness of the antenna. In order to characterize the superconducting Bi2212 single crystal with antenna structure, a-b-axis resistance versus temperature (R-T) were measured in a He flow cryostat before bolometric measurements. The details of the characterization will be given in the following sections.

4.1.1. Optical Microscope Images

Using optical microscopy to image the device is very beneficial in terms of having an idea about the surface to examine the samples. In addition, this characterization provides us some useful information about the quality of the e-beam lithography process. In other words, some problems may come from the lithography and etching process such as remaining of photoresist skin after etching or excess or insufficient etching and contamination onto the surface of the crystal. All pre-characterization technique of the each step of sample fabrication is very useful to understand any problems on the process.

Before starting the e-beam lithography process, Bi2212 crystals are cleaved using a scotch tape to obtain a fresh and smooth surface and after this they are annealed. It can be obviously seen from the Figure 4.1 which are the cleaved crystals have very smooth and clean surface.

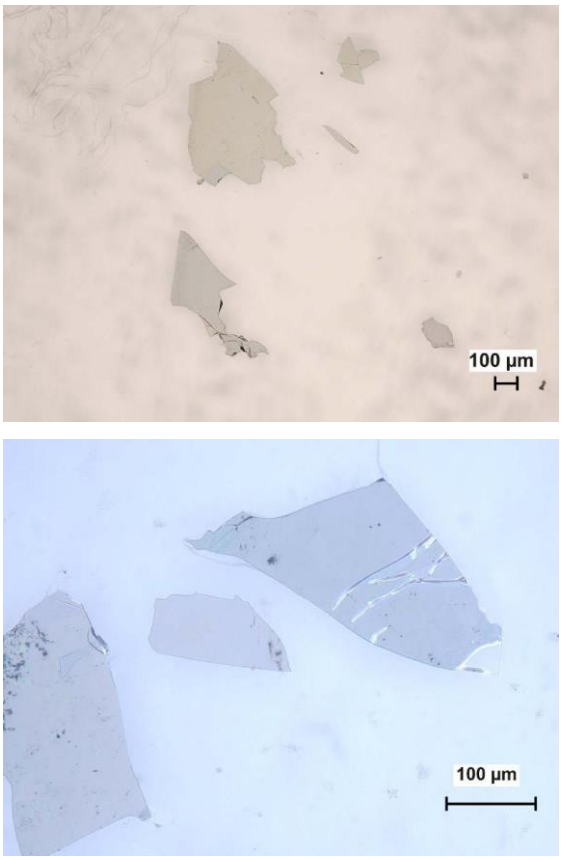

Figure 4.1. Optical images of crystals on sapphire substrates

Finally, in order to determine superconducting properties of crystal, we have placed four copper wires onto the crystal corners and measured the R-T measurement as can be seen in Figure 4.2.

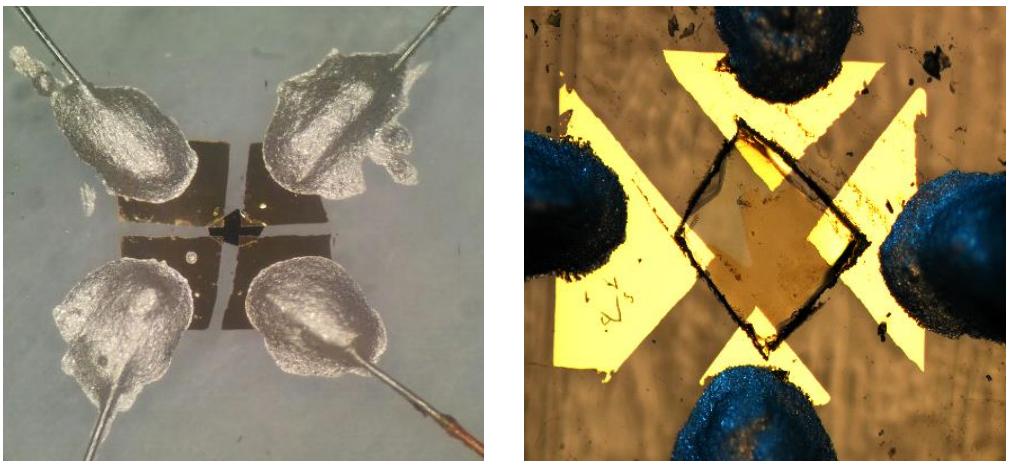

Figure 4.2. Optical images of samples with contacts

Log-periodic antenna pattern which is our design shown in Figure 4.3.

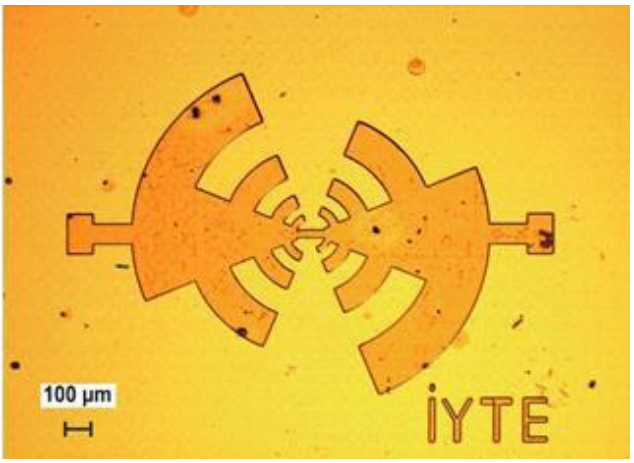

Figure 4.3. The log-periodic antenna has been created in E-beam lithography

4.1.2. SEM and Profilometer Results

We have done the SEM analysis of the Bi2212 crystal to see smooth and clean surface. Surface profilometer are used to determine the exact dimensions of samples.

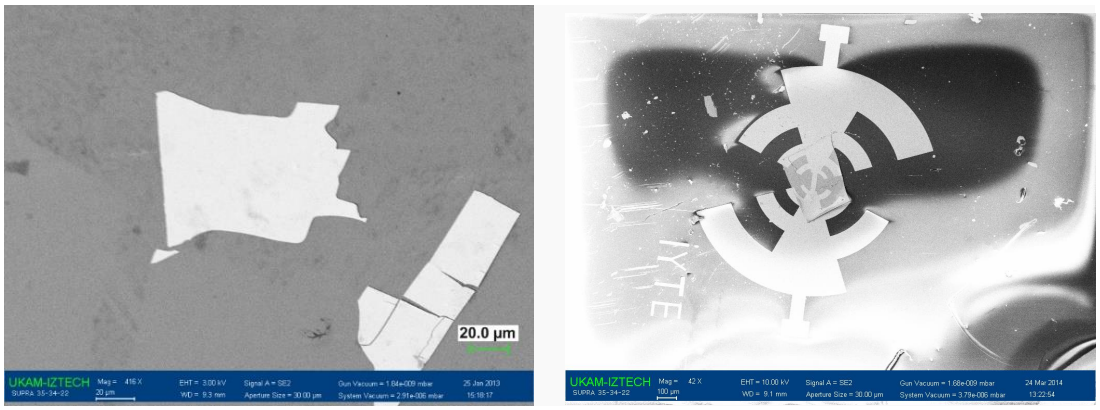

Figure 4.4. SEM images of thinned Bi2212 crystal and log-periodic antenna on it

Dimensions of the log-periodic antenna shown in the Figure 4.5.

Figure 4.5. SEM images of antenna with dimensions on Bi2212 thin film

4.2. Electrical Measurement Results

After we have fabricated the sample with 150 nm Au layer, four-probe contacts were taken to measure a-b-axis resistance versus temperature (R-T) in a (He) Helium flow cryostat. In this section, the details of the R-T measurements will be mentioned.

4.2.1. Temperature Dependence of a-b-axis Resistance in Bi2212

Temperature dependence of a-b-axis resistance from Bi-2212 crystal is observed using a closed cycle Helium cooling. As seen in Table 4.6, the transition temperature values of some chosen samples in many samples placed in this thesis. The transition temperature values are different because of oxygen doping levels and crystal quality. Figures of temperature dependence of a-b axis resistance measurement represent that all samples show exponentially decreasing resistance from room temperature to transition temperature. When the temperature is reached to the transition temperature, a sharp drop is observed. Moreover, the ratios of R_{Tc}/ R_{300K} are changing between 0.46 and 1.17 for all fabricated crystals. When the temperature is below the critical temperature of the Bi-2212 crystal, there is an increase in resistance of the sample due to the contact resistance coming from four-point measurement configuration and the interface between the gold layers.

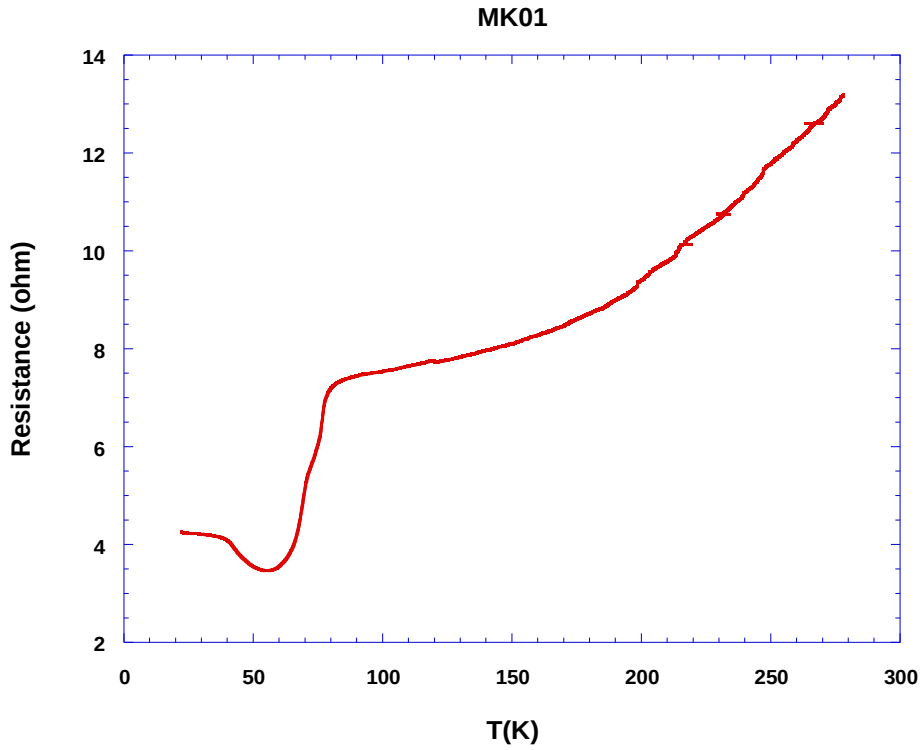

Figure 4.6. R-T measurement of the sample of MK01 with four-point contacts

The Figure 4.6 and Table 4.1 belongs to the MK01 sample, which is fabricated on annealed Bi2212 crsytal. The onset of critical temperature of the crystal is 79.46 K. The R(Tc)/R(300 K) value is 0.54.

Table 4.1. Electrical properties of thinned sample MK01

	R_{Tc} (onset) (ohm)	$R_{300\ K}$ (ohm)	$R_{contact}$ (ohm)	$R_{Tc}/R_{300\ K}$	T_c (onset)	ΔT_c (K)
MK01	7.15	13.21	3.46	0.54	79.46	24.41

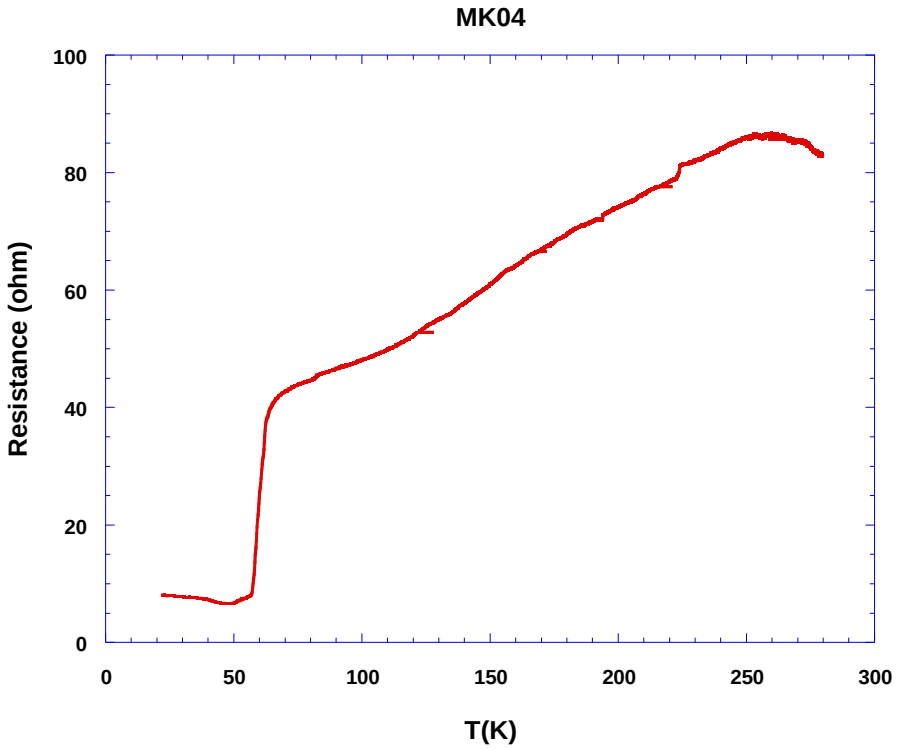

Figure 4.7. R-T measurement of the sample of MK04 with four-point contacts

The Figure 4.7 and Table 4.2 belongs to the MK04 sample, which is fabricated on annealed Bi2212 crsytal. The onset of critical temperature of the crystal is 63.41 K. The R(Tc)/R(300 K) value is 0.46.

Table 4.2. Electrical properties of thinned sample MK04

	R_{Tc} (onset) (ohm)	$R_{300\ K}$ (ohm)	$R_{contact}$ (ohm)	$R_{Tc}/R_{300\ K}$	T_c (onset)	ΔT_c (K)
MK04	38.71	83.33	8.06	0.46	63.41	6.65

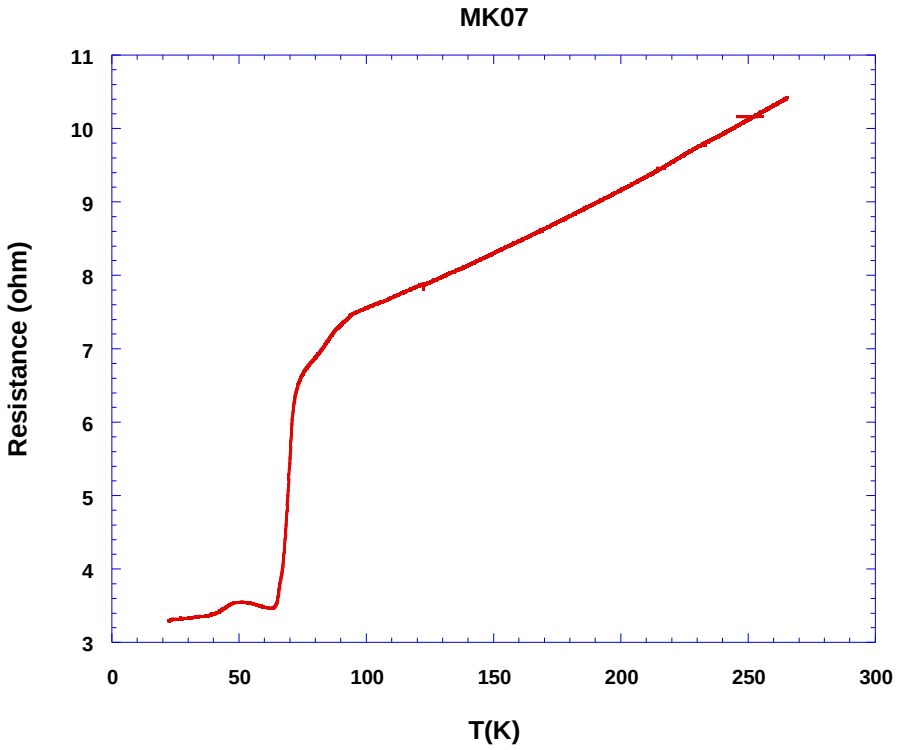

Figure 4.8. R-T measurement of the sample of MK07 with four-point contacts

The Figure 4.8 and Table 4.3 belongs to the MK07 sample, which is fabricated on annealed Bi2212 crsytal. The onset of critical temperature of the crystal is 73.86 K. The R(Tc)/R(300 K) value is 0.63.

Table 4.3. Electrical properties of thinned sample MK07

	R_{Tc} (onset) (ohm)	$R_{300\ K}$ (ohm)	$R_{contact}$ (ohm)	$R_{Tc}/R_{300\ K}$	T_c (onset)	ΔT_c (K)
MK07	6.58	10.43	3.47	0.63	73.86	9.66

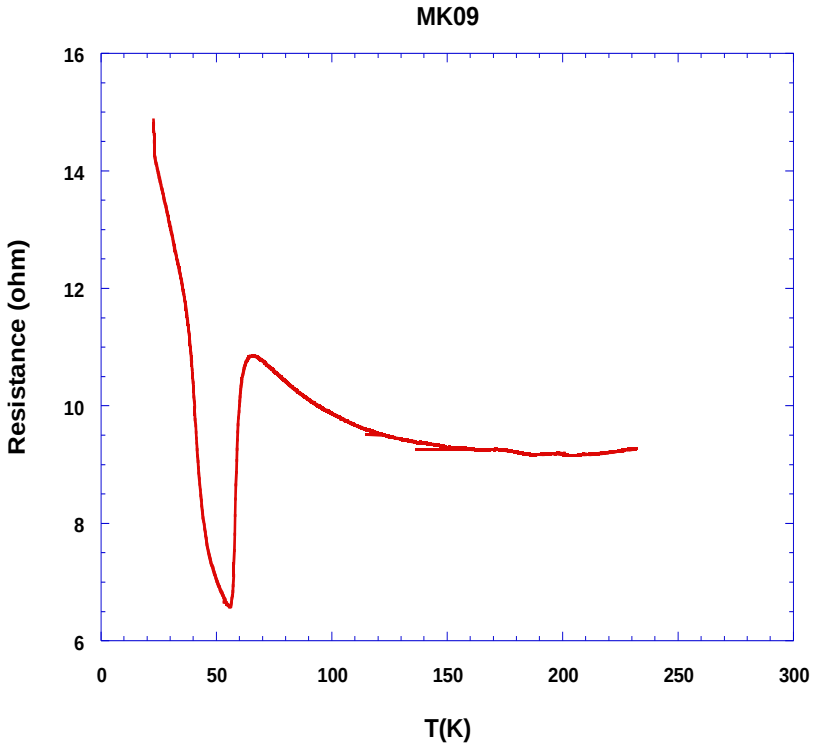

Figure 4.9. R-T measurement of the formed contact resistance of the sample MK09

The Figure 4.9 and Table 4.4 belongs to the MK09 sample, which is fabricated on annealed Bi2212 crsytal. The onset of critical temperature of the crystal is 65.90 K. The R(Tc)/R(300 K) value is 1.17. The contact resistance formed on this sample after the resistance decrease finishing depends on the oxygen doping level and crystal quality.

Table 4.4. Electrical properties of thinned sample MK09

	R_{Tc} (onset) (ohm)	**$R_{300\ K}$ (ohm)**	**$R_{contact}$ (ohm)**	**$R_{Tc}/R_{300\ K}$**	**T_c (onset)**	**ΔT_c (K)**
MK09	10.86	9.28	6.58	1.17	65.90	10.01

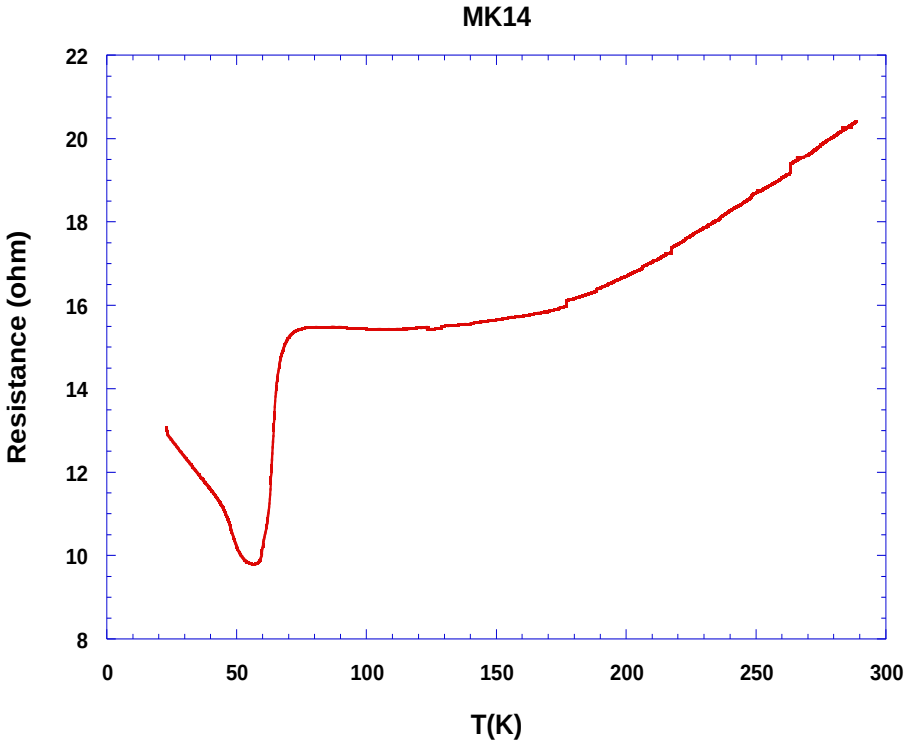

Figure 4.10. R-T of the sample of MK14 with four-point contacts

The Figure 4.10 and Table 4.5 belongs to the MK14 sample, which is fabricated on annealed Bi2212 crystal. The onset of critical temperature of the crystal is 73.75 K. The R(Tc)/R(300 K) value is 0.75.

Table 4.5. Electrical properties of thinned sample MK14

	R_{Tc} (onset) (ohm)	$R_{300\ K}$ (ohm)	$R_{contact}$ (ohm)	$R_{Tc}/R_{300\ K}$	T_c (onset)	ΔT_c (K)
MK14	15.39	20.41	9.79	0.75	73.55	14.38

Table 4.6. Electrical properties of chosen thinned Bi2212 single crystals

	R_{Tc} (onset) (ohm)	$R_{300\ K}$ (ohm)	$R_{contact}$ (ohm)	$R_{Tc}/R_{300\ K}$	T_c (onset)	ΔT_c (K)
MK09	10.86	9.28	6.58	1.17	65.90	10.01
MK01	7.15	13.21	3.46	0.54	79.46	24.41
MK04	38.71	83.33	8.06	0.46	63.41	6.65
MK07	6.58	10.43	3.47	0.63	73.86	9.66
MK14	15.39	20.41	9.79	0.75	73.55	14.38

The Table 4.6 belongs to chosen Bi2212 samples, which are annealed with air atmosphere. The onsets of critical temperature of the crystals are 65.9, 79.46, 63.41, 73.86 and 73.75 K. The $R_{Tc}/R_{300\ K}$ values are 1.17, 0.57, 0.46, 0.63 and 0.75 respectively.

CHAPTER 5

CONCLUSION

Since terahertz (THz) waves can pass through materials like clothing, plastic, wood, ceramic, leather and without any harm to the body, it can be used for characterization, detection and 3D imaging of these materials. THz application area expands day by day such as high-speed wireless communications, medical imaging, security in airports and shopping centres and detection of chemical and biological materials. Rapidly increasing applications of the electromagnetic waves (EM) in the undeveloped terahertz frequency (0.1-10 THz) range requires a well understandings of efficient terahertz wave detection. Today, there are several deficiencies in different types of bolometers that are used for detection of THz waves because they require very difficult and costly cryogenic spending, detectivity has to be high and response time should be low. In this work, in order to decrease the cryogenic cost, to get higher detectivity and small response time we have fabricated thinned Bi2212 single crystal for using in detection of terahertz wave.

Firstly, we have cleaved the Bi2212 single crystal by the mechanical exfoliation until reach the smooth and clean surface and these thinned crystals were glued on the sapphire substrate. After the cleaved process, chemical process via chloroform etchant was applied on samples for the removing scotch tape. Then, these samples were annealed at 400^{o}C about one hour for adjusting the oxygen doping level and after shadowing middle of the crystals with aluminium foil, Au layer with the thickness of 150 nm was thermally deposited on the thinned and annealed crystals. Afterwards, they were annealed again at 425^{o}C about thirty minutes to decrease the contact resistivity. Finally, we have contacted the Au wire on the Au layer with good thermal and electrical conductor silver epoxy. After four probes contacts were made, ab-axis resistance versus temperature (R–T) measurements were performed. The experimental measurements were clearly defined in CHAPTER 3.

On the other hand, we have designed the log-periodic antenna pattern using electron beam lithography, clean room process and ion beam etching techniques. The aim of these pattern supplies the high detectivity of THz waves with small noise equivalent

power (NEP) and small sensitivity time. Also we have fabricated and characterized the cryostat for this project. Cryostat being tested while in this time placed in the vacuum environment of how long the liquid nitrogen has been found to be contained within cryostat. This determination is made by determining the temperature inside cryostat from the temperature controller at vacuum environment with liquid nitrogen. Cryostat liquid nitrogen reservoir contains about 3 liters. Nitrogen has been found to be maintained for about 22 hours in the system. Then accounts for the further improvement of this time, the liquid nitrogen reservoir was coated with 15 μm thickness metallized film for 4 times. Application metallized film was reduced evaporation rate from 0.15 liter/hour to 0.085 liter/hour at the system is not running. The resulting ratio of liquid nitrogen is kept for 30 hours at a temperature of 77 K in the chamber. The vacuum is $1.0x10^{-4}$ Torr before being placed liquid nitrogen and the vacuum decreases to $5.8x10^{-5}$ Torr with cooling process.

When we look at R-T graphs of fabricated Bi2212 single crystal, sharp phase transitions from normal state to superconducting state are seen. Figures of temperature dependence of a-b axis resistance measurement represent that all samples show exponentially decreasing resistance from room temperature to transition temperature. When the temperature is reached to the transition temperature, a sharp drop is observed. Moreover, the onsets of the critical temperatures are generally between 63 K and 80 K and the ratios of R_{Tc}/R_{300K} are changing between 0.46 and 1.17 for all fabricated crystals. We reached the optimum electrical values that were aimed at the beginning of the project. Because working temperature of our cryostat about 77 K and critical temperature of our samples should be higher than 77 K. After all works on these thesis, we conclude that one can produce crystals having transition temperature higher than the 77 K.

REFERENCES

Al'ber, Y.I., A. Andronov, V. Valov, V. Kozlov, and I. Ryazantseva. 1976. Hot electron population inversion and cyclotron resonance negative differential conductivity in semiconductors. *Solid State Communications*. 19:955-959.

Anders, S., T. May, V. Zakosarenko, M. Starkloff, G. Zieger, and H.-G. Meyer. 2009. Structured SiN membranes as platform for cryogenic bolometers. *Microelectronic engineering*. 86:913-915.

Andrews, D., W. Brucksch Jr, W. Ziegler, and E. Blanchard. 2004. Attenuated Superconductors I. For Measuring Infra-Red Radiation. *Review of Scientific Instruments*. 13:281-292.

Arnone, D., C. Ciesla, and M. Pepper. 2000. Terahertz imaging comes into view. *Physics World*. 4:35-40.

Ashley, J.R., and F. Palka. 1973. Transmission cavity and injection stabilization of an X-band transferred electron oscillator. *In* Microwave Symposium, 1973 IEEE G-MTT International. IEEE. 181-182.

Auston, D.H. 1983. Impulse response of photoconductors in transmission lines. *Quantum Electronics, IEEE Journal of*. 19:639-648.

"Background Physics," last modified July 12, 2006, http://hoffman.physics.harvard.edu/materials/organic/background.php

Balanis, C.A. 2012. Antenna theory: analysis and design. John Wiley & Sons.

Bednorz, J.G., and K.A. Müller. 1986. Possible highT c superconductivity in the Ba− La− Cu− O system. *Zeitschrift für Physik B Condensed Matter*. 64:189-193.

Bergmann, G. 1984. Weak localization in thin films: a time-of-flight experiment with conduction electrons. *Physics Reports*. 107:1-58.

Bock, J., D. Chen, P. Mauskopf, and A. Lange. 1995. A novel bolometer for infrared and millimeter-wave astrophysics. *Space Science Reviews*. 74:229-235.

Brown, E., F. Smith, and K. McIntosh. 1993. Coherent millimeter-wave generation by heterodyne conversion in low-temperature-grown GaAs photoconductors. *Journal of Applied Physics*. 73:1480-1484.

Callen, H.B., and T.A. Welton. 1951. Irreversibility and generalized noise. *Physical Review*. 83:34-40.

Chu, C., P. Hor, R. Meng, L. Gao, Z. Huang, Wang, and YQ. 1987. Evidence for superconductivity above 40 K in the La-Ba-Cu-O compound system. *Physical Review Letters*. 58:405-407.

Cibella, S., M. Ortolani, R. Leoni, G. Torrioli, L. Mahler, J.-H. Xu, A. Tredicucci, H. Beere, and D. Ritchie. 2009. Wide dynamic range terahertz detector pixel for active spectroscopic imaging with quantum cascade lasers. *Applied Physics Letters*. 95:213501.

"Classical concept of quantum-cascade lasers" 2013, http://www.wsi.tum.de/Research/AmanngroupE26/AreasofResearch/QuantumCascadeLasers/tabid/111/Default.aspx

"Crystal Growth," last modified October 22, 2001, http://people.seas.harvard.edu/~jones/es154/lectures/lecture_2/materials/materials.html

De Maagt, P., P.H. Bolivar, and C. Mann. 2005. Terahertz science, engineering and systems—From space to earth applications. *Encyclopedia of RF and Microwave Engineering*.

"Disorder in Unconventional Superconductors,1 last modified February 15, 2003, http://www.phys.ufl.edu/~pjh/research/disorder.html

DuHamel, R., and D. Isbell. 1957. Broadband logarithmically periodic antenna structures. *In* IRE International Convention Record. Vol. 5. IEEE. 119-128.

Faist, J., F. Capasso, D.L. Sivco, C. Sirtori, A.L. Hutchinson, and A.Y. Cho. 1994. Quantum Cascade Laser. *Science*. 264:553-556.

Feigelson, R., D. Gazit, D. Fork, and T. Geballe. 1988. Superconducting Bi-Ca-Sr-Cu-O fibers grown by the laser-heated pedestal growth method. *Science*. 240:1642-1645.

Ferguson, B., and X.-C. Zhang. 2002. Materials for terahertz science and technology. *Nature materials*. 1:26-33.

Fleming, J. 1974. High-resolution submillimeter-wave Fourier-transform spectrometry of gases. *IEEE Transactions on Microwave Theory Techniques*. 22:1023-1025.

Fox, M., and G.F. Bertsch. 2002. Optical properties of solids. *American Journal of Physics*. 70:1269-1270.

Gao, L., Y.Y. Xue, F. Chen, Q. Xiong, R.L. Meng, D. Ramirez, C.W. Chu, J.H. Eggert, and H.K. Mao. 1994. Superconductivity up to 164-K in $HgBa_2Ca_{m-1}Cu_mO_{2m+2+\delta}$ (m=1,2, and 3) under Quasi-Hydrostatic Pressures. *Physical Review B*. 50:4260-4263.

Genoud, J.-Y., G. Triscone, A. Junod, T. Tsukamoto, and J. Muller. 1995. Reversible magnetization as a function of the oxygen concentration in Bi-2212 superconducting ceramics. *Physica C: Superconductivity*. 242:143-154.

Giaever, I. 1960. Electron tunneling between two superconductors. *Physical Review Letters*. 5:464-466.

Gladkova, N.D., G. Petrova, N. Nikulin, S. Radenska-Lopovok, L. Snopova, Y.P. Chumakov, V. Nasonova, V. Gelikonov, G. Gelikonov, and R. Kuranov. 2000. In vivo optical coherence tomography imaging of human skin: norm and pathology. *Skin Research and Technology*. 6:6-16.

"Golay Cell," last modified September 10, 2014, http://en.wikipedia.org/wiki/Golay_cell

González, F., and G. Boreman. 2005. Comparison of dipole, bowtie, spiral and log-periodic IR antennas. *Infrared physics & technology*. 46:418-428.

Gorkov, L.P. 1959. Microscopic derivation of the Ginzburg-Landau equations in the theory of superconductivity. *Sov. Phys. JETP*. 9:1364-1367.

Gousev, Y.P., A. Semenov, G. Gol'Tsman, A. Sergeev, and E. Gershenzon. 1994. Electron-phonon interaction in disordered NbN films. *Physica B: Condensed Matter*. 194:1355-1356.

Gregory, I., W. Tribe, B. Cole, C. Baker, M. Evans, I. Bradley, E. Linfield, A. Davies, and M. Missous. 2004. Phase sensitive continuous-wave THz imaging using diode lasers. *Electronics Letters*. 40:143-145.

Gregory, I.S., C. Baker, W.R. Tribe, I.V. Bradley, M.J. Evans, E.H. Linfield, G. Davies, and M. Missous. 2005. Optimization of photomixers and antennas for continuous-wave terahertz emission. *Quantum Electronics, IEEE Journal of*. 41:717-728.

Grosse, E. 2002. THz radiation from free electron lasers and its potential for cell and tissue studies. *Physics in medicine and biology*. 47:3755.

Hazen, R., L. Finger, R. Angel, C. Prewitt, N. Ross, C. Hadidiacos, P. Heaney, D. Veblen, Z. Sheng, and A. El Ali. 1988. 100-K superconducting phases in the Tl-Ca-Ba-Cu-O system. *Physical review letters*. 60:1657.

Irwin, K. 1995. An application of electrothermal feedback for high resolution cryogenic particle detection. *Applied Physics Letters*. 66:1998-2000.

Isbell, D. 1960. Log periodic dipole arrays. *Antennas and Propagation, IRE Transactions on*. 8:260-267.

Jackson, J.B., J. Bowen, G. Walker, J. Labaune, G. Mourou, M. Menu, and K. Fukunaga. 2011. A survey of terahertz applications in cultural heritage conservation science.

Jin, S., T.H. Tiefel, R.C. Sherwood, R.B. van Dover, M.E. Davis, G.W. Kammlott, and R.A. Fastnacht. 1988. Melt-textured growth of polycrystalline $YBa_2Cu_3O_{7-\delta}$ with high transport J_c at 77 K. *Physical Review B*. 37:7850-7853.

Josephson, B.D. 1962. Possible new effects in superconductive tunnelling. *Physics Letters*. 1:251-253.

Kakeya, I., K. Fukui, K. Kawamata, T. Yamamoto, and K. Kadowaki. 2008. Quantum oscillation of the c-axis resistivity due to entrance of pancake vortices into micro-

fabricated $Bi_2Sr_2CaCu_2O_{8+\delta}$ intrinsic Josephson junctions. *Physica C: Superconductivity*. 468:669-673.

Kamihara, Y., H. Hiramatsu, M. Hirano, R. Kawamura, H. Yanagi, T. Kamiya, and H. Hosono. 2006. Iron-based layered superconductor: LaOFeP. *Journal of the American Chemical Society*. 128:10012-10013.

Kato, R., S. Kondo, T. Igo, T. Okita, T. Konishi, S. Suemine, S. Okuda, and G. Isoyama. 2000. Lasing at 150 mu m wavelength and measurement of the characteristics of the free-electron laser at ISIR, Osaka University. *Nuclear Instruments & Methods in Physics Research Section a-Accelerators Spectrometers Detectors and Associated Equipment*. 445:169-172.

Katsui, A. 1988. Crystal growth of superconducting Bi-Sr-Ca-Cu-O compounds from KCl solution. *Japanese journal of applied physics*. 27:L844.

Kawase, K. 2004. Terahertz imaging for drug detection and large-scale integrated circuit inspection. *Optics and photonics news*. 15:34-39.

Kerecman, A.J. 1973. The Tungsten-P Type Silicon Point Contact Diode. *In* Microwave Symposium, 1973 IEEE G-MTT International. IEEE. 30-34.

Kerr, A.R. 1999. Suggestions for revised definitions of noise quantities, including quantum effects. *Microwave Theory and Techniques, IEEE Transactions on*. 47:325-329.

Kittel, C., and P. McEuen. 1986. Introduction to solid state physics. Wiley New York.

Krishna, M.G., S.D. Kshirsagar, and S.P. Tewari. Terahertz Emitters, Detectors and Sensors: Current Status and Future Prospects.

Landau, L., and V. Ginzburg. 1950. On the theory of superconductivity. *Journal of Experimental and Theoretical Physics (USSR)*. 20:1064.

Langley, S. 1898. The bolometer. *Nature*. 57:53.

Langley, S.P. 1881. The actinic balance. *American Journal of Science*:187-198.

Lee, S.-F., J.M. Gildemeister, W. Holmes, A.T. Lee, and P.L. Richards. 1998. Voltage-biased superconducting transition-edge bolometer with strong electrothermal feedback operated at 370 mK. *Applied Optics*. 37:3391-3397.

Lee, Y.-S. 2009. Principles of Terahertz Science and Technology: Proceedings of the International Conference, Held in Mainz, Germany, June 5-9, 1979. Springer.

Low, F., and A. Hoffman. 1963. The detectivity of cryogenic bolometers. *Applied Optics*. 2:649-650.

Maeda, H., Y. Tanaka, M. Fukutomi, and T. Asano. 1988. A new high-T_c oxide superconductor without a rare earth element. *Japanese Journal of Applied Physics*. 27:L209.

Meissner, W., and R. Ochsenfeld. 1933. A new effect in penetration of superconductors. *Die Naturwissenschaften*. 21:787-788.

Mendis, R., C. Sydlo, J. Sigmund, M. Feiginov, P. Meissner, and H.L. Hartnagel. 2004. Tunable CW-THz system with a log-periodic photoconductive emitter. *Solid-State Electronics*. 48:2041-2045.

Michishita, K., Y.H. Ikuhara, and Y. Kubo. 1996. Bi-Based Superconductor Fabricated by the Fioating-Zone Method. *Bismuth-Based High-Temperature Superconductors*:253.

Mittleman, D., M. Gupta, R. Neelamani, R. Baraniuk, J. Rudd, and M. Koch. 1999. Recent advances in terahertz imaging. *Applied Physics B*. 68:1085-1094.

Miyakawa, N., P. Guptasarma, J. Zasadzinski, D. Hinks, and K. Gray. 1998. Strong dependence of the superconducting gap on oxygen doping from tunneling measurements on $Bi_2Sr_2CaCu_2O_{8-\delta}$. *Physical review letters*. 80:157.

Mueller, E.R. 2006. Terahertz Radiation Sources for Imaging and Sensing Applications-New techniques are being used to generate emissions at terahertz frequencies. *Photonics Spectra*. 40:60-69.

Nagamatsu, J., N. Nakagawa, T. Muranaka, Y. Zenitani, and J. Akimitsu. 2001. Superconductivity at 39 K in magnesium diboride. *Nature*. 410:63-64.

Onnes, H.K. 1911. Disappearance of the electrical resistance of mercury at helium temperatures. *Akad. Van Wetenschappen*.

Ono, A., S. Sueno, and F.P. Okamura. 1988. Preparation and properties of single crystals of the high-T_c oxide superconductor in the Bi-Sr-Ca-Cu-O system. *Japanese journal of applied physics*. 27:L786.

Ozyuzer, L., A. Koshelev, C. Kurter, N. Gopalsami, Q. Li, M. Tachiki, K. Kadowaki, T. Yamamoto, H. Minami, and H. Yamaguchi. 2007. Emission of coherent THz radiation from superconductors. *Science*. 318:1291-1293.

Pawar, A.Y., D.D. Sonawane, K.B. Erande, and D.V. Derle. 2013. Terahertz technology and its applications. *Drug Invention Today*. 5.

Perrin, N., and C. Vanneste. 1983. Response of superconducting films to a periodic optical irradiation. *Physical Review B*. 28:5150.

Ren, Z.-A., W. Lu, J. Yang, W. Yi, X.-L. Shen, Z.-C. Li, G.-C. Che, X.-L. Dong, L.-L. Sun, and F. Zhou. 2008. Superconductivity at 55 K in iron-based F-doped layered quaternary compound Sm $[O_{1-x}F_x]$ FeAs. *arXiv preprint arXiv:0804.2053*.

Revcolevschi, A., and J. Jegoudez. 1997. Growth of large high-T_c single crystals by the floating zone method: A review. *Progress in materials science*. 42:321-339.

Richards, P. 1994. Bolometers for infrared and millimeter waves. *Journal of Applied Physics*. 76:1-24.

Rogalski, A., and F. Sizov. 2011. Terahertz detectors and focal plane arrays. *Opto-Electronics Review*. 19:346-404.

Saijo, H., M. Morimoto, T. Kiwa, and M. Tonouchi. 2001. Terahertz emission properties from YBCO thin film log-periodic antennas. *Physica C: Superconductivity*. 362:319-323.

Schilling, A., M. Cantoni, J. Guo, and H. Ott. 1993. Superconductivity above 130 K in the Hg-Ba-Ca-Cu-O system. *Nature*. 363:56-58.

Semenov, A.D., G.N. Gol'tsman, and R. Sobolewski. 2002. Hot-electron effect in superconductors and its applications for radiation sensors. *Superconductor Science and Technology*. 15:R1.

Shishido, T., D. Shindo, K. Ukei, T. Sasaki, N. Toyota, and T. Fukuda. 1989. Growth of single crystals in the Bi-Sr-Ca-Cu-O system using KCl as a flux. *Japanese Journal of Applied Physics*. 28:L791.

Sischka, F. 2002. Basics of S-Parameters, part 1. *Agilent Technologies Characterization Handbook, May*.

Sizov, F., and A. Rogalski. 2010. THz detectors. *Progress in Quantum Electronics*. 34:278-347.

Smith, P.R., D.H. Auston, and M.C. Nuss. 1988. Subpicosecond photoconducting dipole antennas. *Quantum Electronics, IEEE Journal of*. 24:255-260.

Stockhausen, A. 2013. Optimization of Hot-Electron Bolometers for THz Radiation. KIT Scientific Publishing.

Subrahmanyam, A., Y.B.K. Reddy, and C. Nagendra. 2008. Nano-vanadium oxide thin films in mixed phase for microbolometer applications. *Journal of Physics D: Applied Physics*. 41:195108.

"Superconductivity," last modified March 14, 2009, http://users-phys.au.dk/philip/pictures/physicsfigures/physicsfigures.html

Tachiki, M., S. Fukuya, and T. Koyama. 2009. Mechanism of terahertz electromagnetic wave emission from intrinsic Josephson junctions. *Physical review letters*. 102:127002.

Taillefer, L., B. Lussier, R. Gagnon, K. Behnia, and H. Aubin. 1997. Universal heat conduction in $YBa_2Cu_3O_{6.9}$. *Physical review letters*. 79:483.

Takahashi, H., K. Igawa, K. Arii, Y. Kamihara, M. Hirano, and H. Hosono. 2008. Superconductivity at 43 K in an iron-based layered compound $LaO_{1-x}F_xFeAs$. *Nature*. 453:376-378.

Takekawa, S., H. Nozaki, A. Umezono, K. Kosuda, and M. Kobayashi. 1988. Single crystal growth of the superconductor $Bi_{2.0}(Bi_{0.2}Sr_{1.8}Ca_{1.0})Cu_{2.0}O_8$. *Journal of crystal growth*. 92:687-690.

Tanaka, H., M. Nakamura, and S. Kishida. 2001. Growth of $Bi_2Sr_2CaCu_2O_y$ single crystals by a modified vertical Bridgman method. *Physica C: Superconductivity*. 357:722-725.

Thiele, W.S.G., and W.L. Stutzman. 1981. Antenna theory and design. *Sections*. 7.

Tonouchi, M. 2007. Cutting-edge terahertz technology. *Nature photonics*. 1:97-105.

Torres, A., A. Kosarev, M. García Cruz, and R. Ambrosio. 2003. Uncooled micro-bolometer based on amorphous germanium film. *Journal of non-crystalline solids*. 329:179-183.

Van Exter, M., C. Fattinger, and D. Grischkowsky. 1989. High-brightness terahertz beams characterized with an ultrafast detector. *Applied Physics Letters*. 55:337-339.

Van Neste, C.W., L.R. Senesac, and T. Thundat. 2008. Standoff photoacoustic spectroscopy. *Applied Physics Letters*. 92:234102.

Wang, X., L. You, D. Liu, C. Lin, X. Xie, and M. Jiang. 2012. Thin-film-like BSCCO single crystals made by mechanical exfoliation. *Physica C: Superconductivity*. 474:13-17.

Watanabe, T., T. Fujii, and A. Matsuda. 1997. Anisotropic Resistivities of Precisely Oxygen Controlled Single-Crystal $Bi_2Sr_2CaCu_2O_{8+\delta}$: Systematic Study on``Spin Gap"Effect. *Physical review letters*. 79:2113.

Wellstood, F., C. Urbina, and J. Clarke. 1994. Hot-electron effects in metals. *Physical Review B*. 49:5942.

Wesche, R. 1998. High-temperature superconductors: materials, properties, and applications. Kluwer Academic Publishers.

Woodward, R.M., B.E. Cole, V.P. Wallace, R.J. Pye, D.D. Arnone, E.H. Linfield, and M. Pepper. 2002. Terahertz pulse imaging in reflection geometry of human skin cancer and skin tissue. *Physics in Medicine and Biology*. 47:3853.

Wu, M.K., J. Ashburn, C. Torng, P.H. Hor, R. Meng, L. Gao, Z. Huang, Y. Wang, and C. Chu. 1987. Superconductivity at 93 K in a new mixed-phase Y-Ba-Cu-O compound system at ambient pressure. *Physical Review Letters*. 58:908-910.

Xie, A., L. van der Meer, and R.H. Austin. 2002. Excited-state lifetimes of far-infrared collective modes in proteins. *Journal of Biological Physics*. 28:147-154.

Yamada, Y., T. Watanabe, and M. Suzuki. 2007. Fabrication and transport properties for cleaved thin film BSCCO single crystals. *Applied Superconductivity, IEEE Transactions on*. 17:3533-3536.

Yasuda, T., T. Kawae, T. Yamashita, T. Uchiyama, I. Iguchi, M. Tonouchi, and S. Takano. 2002. Superconducting properties of $Bi_2Sr_2CaCu_2O_x$ films grown by liquid phase epitaxy. *Physica C: Superconductivity*. 378:1265-1269.

Yurgens, A. 2000. Intrinsic Josephson junctions: recent developments. *Superconductor Science and Technology*. 13:R85-R100.

Zhang, X.C., Y. Jin, and X. Ma. 1992. Coherent measurement of THz optical rectification from electro-optic crystals. *Applied physics letters*. 61:2764-2766.